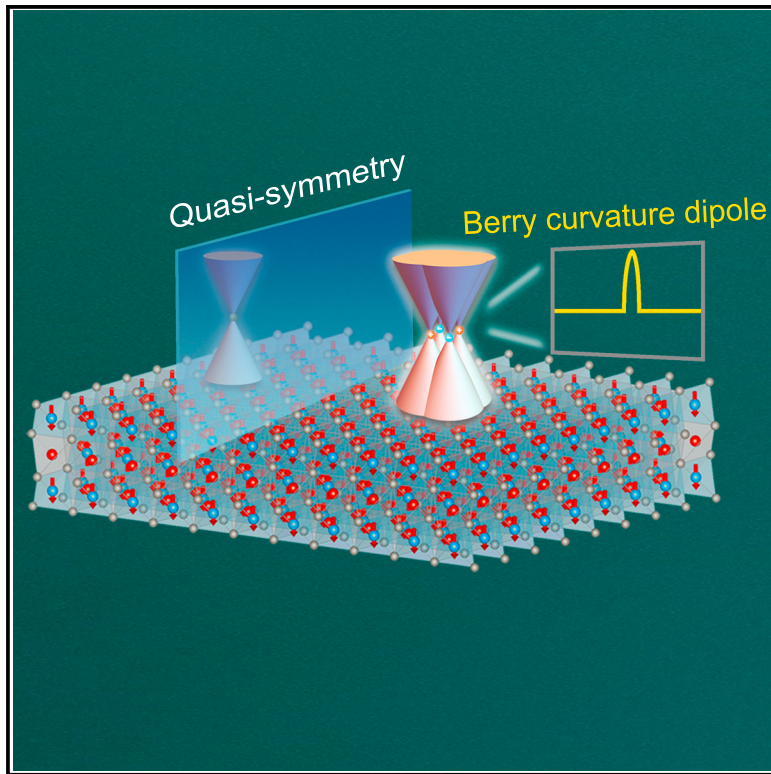


Topological charge quadrupole protected by spin-orbit $U(1)$ quasi-symmetry in antiferromagnet NdBiPt

Graphical abstract



Authors

Ao Zhang, Xiaobing Chen, Jiayu Li, Pengfei Liu, Yuntian Liu, Qihang Liu

Correspondence

liuqh@sustech.edu.cn

In brief

Introducing the mathematical concept of topology to the field of condensed matter has enabled the classification of materials based on their symmetry-protected topological properties. This study presents the topological charge quadrupole found in the half-Heusler antiferromagnet NdBiPt. This unconventional elementary excitation comprises closely packed Weyl points and is protected by a new type of approximate symmetry called quasi-symmetry. The topological charge quadrupole generates a significant nonlinear Hall effect, highlighting pathways for materials with enhanced properties for applications in antiferromagnetic spintronics.

Highlights

- A new type of quasiparticle contains topological Weyl fermions forming a quadrupole
- Topological charge quadrupole is protected by spin-orbit $U(1)$ quasi-symmetry
- Topological charge quadrupole in NdBiPt manifests a significant nonlinear Hall effect

Article

Topological charge quadrupole protected by spin-orbit $U(1)$ quasi-symmetry in antiferromagnet NdBiPt

Ao Zhang,^{1,4} Xiaobing Chen,^{2,1,4} Jiayu Li,¹ Pengfei Liu,¹ Yuntian Liu,¹ and Qihang Liu^{1,2,3,5,*}

¹Department of Physics and Guangdong Basic Research Center of Excellence for Quantum Science, Southern University of Science and Technology, Shenzhen 518055, China

²Quantum Science Center of Guangdong-Hong Kong-Macao Greater Bay Area (Guangdong), Shenzhen 518045, China

³Guangdong Provincial Key Laboratory for Computational Science and Material Design, Southern University of Science and Technology, Shenzhen 518055, China

⁴These authors contributed equally

⁵Lead contact

*Correspondence: liuqh@sustech.edu.cn

<https://doi.org/10.1016/j.newton.2025.100010>

ACCESSIBLE OVERVIEW Topology, a purely mathematical concept, is playing an increasingly important role in condensed matter physics. Materials can now be classified by their topological properties in a manner similar to the classification of geometric shapes, with crystalline symmetry and band topology often being inseparably intertwined. These concepts serve as natural guidelines for searching topological materials. A more recent concept known as quasi-symmetry establishes robust and unconventional topology that extends beyond the above-mentioned symmetry-based classifications, enabling significant topological responses to emerge in magnetic systems. For example, in this paper, the quasi-symmetry concept is applied to the half-Heusler antiferromagnet NdBiPt, unveiling a previously unreported quasiparticle referred to as a topological charge quadrupole. This quasiparticle consists of closely packed 2-fold degenerate Weyl fermions with various topological charges. In electronic transport, a significant nonlinear Hall effect can arise, which can be utilized for detecting magnetic order, thereby providing new possibilities for antiferromagnetic spintronics.

SUMMARY

The interplay of symmetry and topology in crystal solids has given rise to various elementary excitations as quasiparticles. Among these, those with significant Berry-phase-related transport responses are of particular interest. In this study, we predict a type of quasiparticle called a topological charge quadrupole (TCQ), which is analogous to a charge quadrupole but consists of two closely packed pairs of Weyl points in momentum space, specifically in the half-Heusler antiferromagnet NdBiPt. Interestingly, the TCQ is protected by the spin-orbit $U(1)$ quasi-symmetry rather than any exact crystallographic symmetries. This quasi-symmetry restricts the energy splitting induced by symmetry-lowering perturbations to a second-order effect. Furthermore, the closely located Berry curvature sources and sinks in the TCQ lead to a large Berry curvature dipole, resulting in a significant nonlinear Hall effect. Our work opens an avenue for designing unconventional quasiparticles utilizing quasi-symmetries and developing materials with enhanced nonlinear responses.

INTRODUCTION

The investigation of topological semimetals and the discovery of gapless elementary excitations in these materials have been a prosperous area of research in condensed matter physics.^{1–4} Various types of emergent quasiparticles, exemplified by Dirac,^{5–10} Weyl,^{11–19} and other fermions beyond them,^{20–23} have been predicted and observed in solids as low-energy fer-

mionic excitations near the band crossings protected by symmetry and topology. The discovery of these quasiparticles has also led to the use of crystallographic-symmetry-based scenarios, i.e., space groups and magnetic space groups, to classify topological materials.^{24–33} Recently, the classification of quasiparticles has been extended to include spin space groups, allowing for the treatment of magnetic materials with negligible spin-orbit coupling (SOC). This extension predicts various types

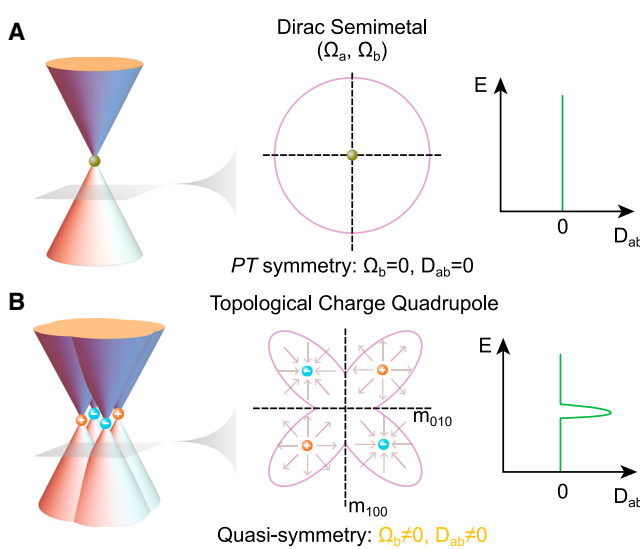


Figure 1. Schematics of the Dirac fermion and the TCQ

(A) A Dirac semimetal protected by PT symmetry exhibits zero Berry curvature (Ω_b) and zero Berry curvature dipole (D_{ab}).
 (B) A topological charge quadrupole is protected by the quasi-symmetry, resulting in a significant Berry curvature and Berry curvature dipole. The orange and blue spheres represent Weyl points with the monopole charges +1 and -1, respectively. The middle images in (A) and (B) represent Fermi surfaces and Berry curvatures of the Dirac cone and topological charge quadrupole (TCQ), respectively.

of multifold band degeneracies and unconventional quasiparticles in both electronic and magnonic spectra.^{34–39} Notably, the topological semimetals of particular interest are those hosting quasiparticles with observable transport responses. One such example is that magnetic Weyl semimetals exhibit the linear and nonlinear anomalous Hall effect^{40–42} induced by Berry curvature. In contrast, Dirac semimetals, protected by PT symmetry (where P and T denote space inversion and time reversal, respectively), exhibit a vanishing Berry curvature throughout momentum space, resulting in no related transport effects (Figure 1A). Therefore, a long-sought goal is to identify ideal materials with topological quasiparticles close to the Fermi level that also exhibit significant transport properties.

In this work, we propose a type of quasiparticle, dubbed the topological charge quadrupole (TCQ), in the noncentrosymmetric half-Heusler compound NdBiPt with a collinear antiferromagnetic (AFM) order. Analogous to the charge quadrupole, the TCQ consists of four closely located Weyl points in momentum space, with two possessing a topological charge of +1 and the other two having a topological charge of -1, as shown in Figure 1B. Interestingly, such a quasiparticle complex is not protected by exact symmetry but rather by a novel spin-orbit $U(1)$ quasi-symmetry.^{43,44} While the electronic structure of NdBiPt closely resembles a Dirac semimetal, the four nearly degenerate Weyl points manifest Berry curvature sources and sinks within a small region of momentum space, leading to a strong Berry curvature dipole (BCD) and nonlinear Hall effects (Figure 1B). The TCQ of NdBiPt results in a significant BCD peak located only 5.8 meV below the Fermi level, with a peak value comparable to those of the T_d

phase of WTe_2 ⁴⁵ and collinear AFM CuMnSb.⁴² Furthermore, the strong dependence of the BCD on the Néel vector can be used for detecting the Néel vector itself. Our work not only reveals the important role of hidden symmetry in predicting new quasiparticles but also provides an approach for designing significant quantum geometric effects in unconventional AFM materials.

RESULTS

TCQ in NdBiPt

Recent neutron diffraction measurements show that NdBiPt accommodates an A-type collinear AFM configuration⁴⁶ along the [001] direction of the nonmagnetic cubic conventional cell below the Néel temperature $T_N = 2.18$ K, resulting in the tetragonal magnetic unit cell with lattice constants $a = b = 4.78$ Å and $c = 6.76$ Å (Figure 2A). The magnetic geometry and the spin-orbit coupling (SOC)-free electronic structure are fully described by its spin space group $G_S = P\bar{4}1m\bar{1}2^{-1}(1/2\ 1/2\ 1/2)^{\infty m1}$ (no. 115.119.2.1), which is identified by the online program FIND-SPINGROUP.^{47,48} In particular, the collinear magnetic order is described by the spin-only group $G_{SO} = {}^{\infty m1} = SO(2) \times Z_2^K$ (only contains pure spin operations), where $SO(2)$ and Z_2^K represent the continuous spin rotations along the collinear spin axis and the mirror symmetry TU in spin space (U is the 2-fold rotation along any axis perpendicular to the collinear spin axis), respectively (see supplemental methods A for detailed symmetry analysis). The density functional theory (DFT)-calculated band structure without SOC is shown in Figure 2C (see methods). Two prominent features are observed. The first one is the double degeneracy throughout the whole Brillouin zone protected by the U_T and $SO(2)$ symmetries,^{39,47} where $\tau = (1/2, 1/2, 1/2)$ is the fractional translation symmetry that connects the two opposite-spin sublattices. Notably, U_T -enforced double degeneracy provides emergent quasiparticles with doubled topological charges from two P -broken spin channels,^{37,38} which differs from the compensated ones enforced by PT symmetry.³⁹ Secondly, a 4-fold degenerate β band (orange line) intersects with a 2-fold degenerate α band (green line), forming a 6-fold degenerate quasiparticle at the $Q(0, 0, 0.006\frac{2\pi}{c})$ point. Such a β band comprises a Dirac nodal line along $-Q - \Gamma - Q$, as shown in Figure 2D, while the nodal line splits off this high-symmetry line (Figure S1).

Since NdBiPt is composed of heavy elements, the corresponding electronic structure with SOC is expected to exhibit significant SOC-induced band splitting as shown in Figure 2E. The electronic structure with SOC is dictated by its magnetic space group $G_M = P\bar{4}n\bar{2}$ (no. 118.314). In the presence of SOC, both U_T and $SO(2)$ symmetries are broken, leading to the spin-polarized non-degenerate bands. However, the bands along the $\Gamma - Z$ direction maintain 2-fold degeneracy, which is protected by 2-fold rotation $\{2_{001}|0\}$ and glide mirror $\{m_{010}|\tau\}$ (see supplemental methods A). Additionally, the 4-fold degenerate β band splits into β_1 and β_2 . Surprisingly, while the SOC gap between α and β_2 ($\Delta E_{\alpha\beta_2}$) at the Q point remarkably reaches 672.4 meV (indicated by the black arrow), an unexpectedly small SOC gap $\Delta E_{\alpha\beta_1} = 9.2$ meV emerges between α and β_1 . To illustrate the evolution of the SOC effect, we present the electronic

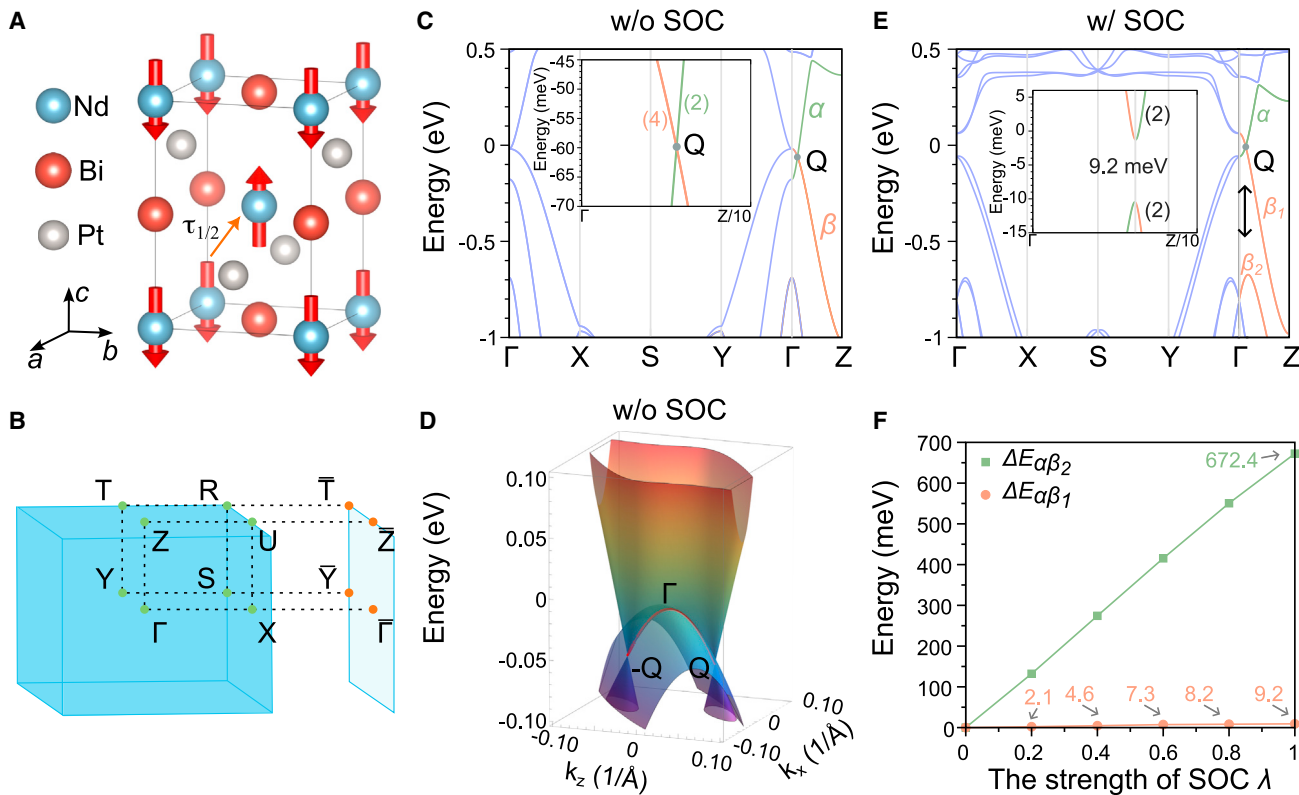


Figure 2. Magnetic structure, BZs, and electronic structures of NdBiPt

(A) The magnetic structure of collinear AFM NdBiPt.
(B) Bulk and surface Brillouin zones (BZs) of NdBiPt.

(C) The electronic structure of NdBiPt without spin-orbit coupling (SOC). The inset shows the degeneracy between α and β bands.

(D) Three-dimensional electronic structure of NdBiPt. The red line denotes the Dirac nodal line within the $k_z - k_x$ plane without SOC.

(E) The electronic structure of NdBiPt with SOC. The inset shows the tiny gap between α and β_1 bands. The green and orange bands denote the α and β_1/β_2 bands, respectively. The black arrow indicates the gap $\Delta E_{\alpha\beta_2}$ between α and β_2 at the Q (0, 0, 0.006) point (fractional coordinates). The Fermi level is set to zero.

structures with varying SOC strengths λ in Figure S2. Specifically, as λ increases, $\Delta E_{\alpha\beta_2}$ exhibits a significant linear increase from 0 to 672.4 meV, while $\Delta E_{\alpha\beta_1}$ increases gradually and eventually reaches 9.2 meV (Figure 2F). The substantial difference between $\Delta E_{\alpha\beta_1}$ and $\Delta E_{\alpha\beta_2}$ cannot be explained by traditional group representation theory because α , β_1 , and β_2 bands share the same two-dimensional irreducible representation \bar{Q}_5 of the little group $G_M^Q = \bar{4}m2'$ at the Q point.

We next look into the fine electronic structure within the tiny gap of $\Delta E_{\alpha\beta_1}$, where multiple Weyl points reside. In the noncentrosymmetric $T\tau$ -AFM NdBiPt, each Weyl point has a $T\tau$ partner of the same chirality. Meanwhile, two glide mirror symmetries, $\{m_{100}|\tau\}$ and $\{m_{010}|\tau\}$, connect Weyl points of opposite chirality. Consequently, an AFM Weyl semimetal with eight Weyl nodes is confirmed by DFT calculations, as shown in Figure 3A. Taking a close look off the Q point, we have uncovered two pairs of Weyl points with charge ± 1 (Figure S3). Due to the tiny gap at Q, these Weyl points form a square with a side length of 0.01 \AA^{-1} , which is only $1/131$ of the in-plane reciprocal lattice parameter. Therefore, such a closely packed configuration of Weyl points forms a TCQ in momentum space. Because of the $T\{2_{001}|\tau\}$ symmetry,

the chirality distributions around Q and $-Q$ points are the same, as shown in Figure 3A. Therefore, in the (001) surface Brillouin zone, the Weyl points are projected pairwise on four different projected positions W_i ($i = 1, 2, 3, 4$) with an effective topological charge of ± 2 . Such a distribution of Weyl points results in two overlapping Fermi rings composed of four individual Fermi arcs and further forms two closed Fermi rings due to band hybridization (see the right image of Figure 3A). We calculate the Fermi arc surface states on the (001) surface, where the two closed Fermi ring surface states are presented in Figure 3B. The smaller Fermi ring connecting the TCQ is further shown in Figure 3C.

Spin-orbit $U(1)$ quasi-symmetry

The key feature of the TCQ is the near-degenerate Weyl points, which cannot be well explained by any exact symmetries. However, recent studies showed that the classical group representation theory could be extended to address the issue of near degeneracy by using quasi-symmetry.^{43,44,49} Different from the general concept of approximate symmetry,⁵⁰ quasi-symmetry refers to the hidden symmetry within a degenerate orbital

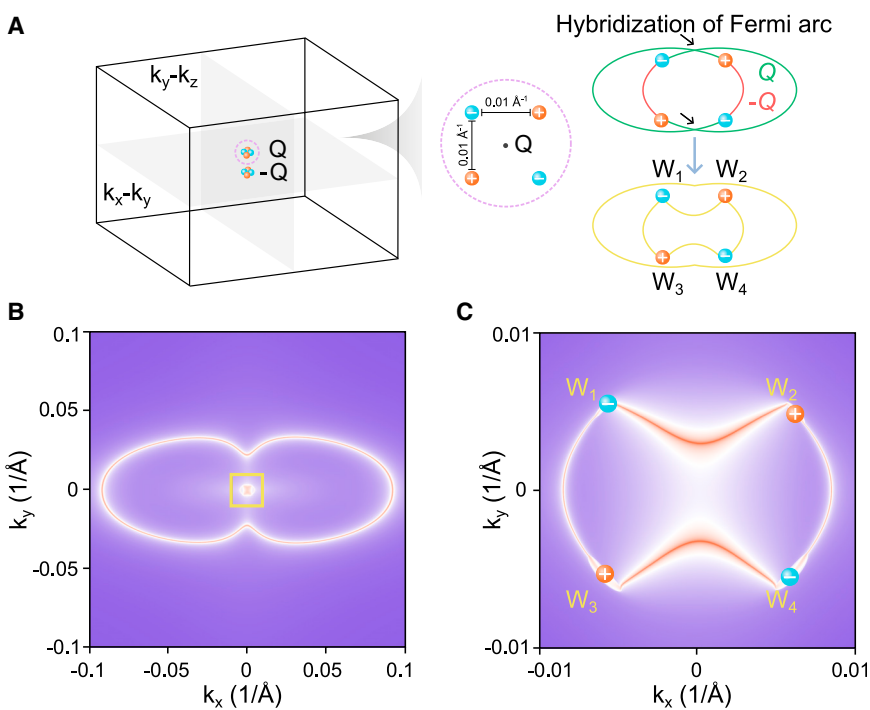


Figure 3. The distribution and Fermi arcs of TCQ

(A) The distribution of TCQ in the Brillouin zone of NdBiPt. The orange and blue spheres represent Weyl points with the monopole charges +1 and -1, respectively. The right image shows a schematic diagram of two closed Fermi rings formed by the hybridization of Fermi arcs. The green and red lines represent the Fermi arcs located at Q and $-Q$, respectively.

(B) The isoenergy surface states enclosing topological charge quadrupole on the $k_x - k_y$ plane at 5.8 meV below the Fermi energy.

(C) An enlarged view of the yellow square is marked in (B).

subspace under an unperturbed Hamiltonian H^0 . This limits the occurrence of the symmetry-lowering term, denoted as H' , to only second-order effects. While the previous studies have primarily focused on nonmagnetic systems, we next demonstrate that the formation of the TCQ in AFM NdBiPt can be attributed to a type of spin-orbit $U(1)$ quasi-symmetry. This symmetry results in a partially lifted band degeneracy under the first-order SOC effect and, thus, a tiny gap when involving the second-order SOC effect at the Q point.

By analyzing the DFT-calculated orbital projection of the bands along the $\Gamma - Z$ direction (Figures S4–S6; Table S2), we can effectively write the α , β_1 , and β_2 bands as

$$\left\{ \begin{array}{l} \alpha = (|l_0, \uparrow\rangle + |l_0, \downarrow\rangle)/\sqrt{2} \\ \beta_1 = (|l_+, \uparrow\rangle + |l_-, \downarrow\rangle)/\sqrt{2} \\ \beta_2 = (|l_-, \uparrow\rangle + |l_+, \downarrow\rangle)/\sqrt{2} \end{array} \right. \quad (\text{Equation 1})$$

where $|l_0$ and $|l_{\pm}$ can be expressed as linear combinations of the atomic orbitals, designated as $|l_0\rangle = \theta|s\rangle + \gamma|p_z\rangle$ and $|l_{\pm}\rangle = \frac{1}{\sqrt{2}}(|u_x\rangle \pm i|u_y\rangle)$, where $|u_{x/y}\rangle = \eta|p_{x/y}\rangle + \delta|d_{xz/yz}\rangle$. In the absence of SOC, the symmetry of the Hamiltonian $H_A^0 = H_k + H_p + H_{mag}$, which includes the kinetic term H_k , the potential term H_p , and the magnetic term H_{mag} , can be described by $G_{H_A^0} = G_S$. The doubly degenerate band α and the 4-fold degenerate band β with irreducible representations $Q_{1,A}^{1/2}(2)$ and $Q_{3,A}^{1/2}Q_{4,A}^{1/2}(4)$ of the little group $G_{H_A^0}^Q = \bar{4}^{-1}m^m2^{\infty}1$ intersect at the Q point as shown in Figure 4A. When including SOC, the β band splits into two doubly degenerate bands β_1 and β_2 . The band crossing between

α and β_1 is gapped (and so is that between α and β_2) because α , β_1 , and β_2 bands share the same magnetic group representation $\bar{Q}_5(2)$ (Figure 4D). We next use the quasi-symmetry theory to elucidate the remarkable difference of two SOC-induced gaps at the Q point, $\Delta E_{\alpha\beta_1}$, and $\Delta E_{\alpha\beta_2}$.

Note that the difference between $\Delta E_{\alpha\beta_1}$ and $\Delta E_{\alpha\beta_2}$ cannot be captured using any group extended by $G_{H_A^0}^Q$, which failed in separating bands β_1 and β_2 (see [supplemental methods B](#)). Interestingly, we find that the $\lambda L_z S_z$ term does not contribute to the two SOC gaps but splits the β band into bands β_1 and β_2 (see [supplemental methods C](#)). Therefore, we consider the unperturbed Hamiltonian $H_B^0 = H_A^0 + \lambda L_z S_z$ and the perturbed Hamiltonian $H_B' = \frac{\lambda}{2}(L_+ S_- + L_- S_+)$. The introduction of $\lambda L_z S_z$ breaks the little group $G_{H_A^0}^Q$ into $G_{H_B'}^Q = \bar{4}^{-2}m^m2^{\infty}1$, thus providing an adequate starting point of three doubly degenerate bands (Figure 4B). Then, we find that the spin-orbit $U(1)$ symmetry $P_q = \{U_z(\theta) \parallel R_z(\theta)\}$, [51,52](#) which represents the simultaneously continuous rotation along the z direction in both spin and lattice space, is not in $G_{H_B'}^Q$ but commutes with H_B' . It transforms the matrix element $\langle \alpha | H_B' | \beta_1 \rangle$ into an additional phase factor, i.e., $\langle \alpha | H_B' | \beta_1 \rangle \xrightarrow{P_q} e^{i\omega(P_q)} \langle \alpha | H_B' | \beta_1 \rangle$, thereby enforcing the first-order SOC effect between α and β_1 bands to be zero.[44](#) In contrast, two elements of $\langle \alpha | H_B' | \beta_2 \rangle$ are transformed as an identity representation (see [supplemental methods D](#)), resulting in a relatively larger gap as shown in Figure 4C. Consequently, the first-order SOC-induced gap at Q is zero between α and β_1 bands, leading to a small second-order gap of 9.2 meV. In contrast, the band crossing of α and β_2 bands is lifted by first-order SOC with 672.4 meV (Figure 4D).

To validate the above quasi-symmetry analysis, we constructed a $k \cdot p$ model near the Γ point (see [supplemental methods E](#)). The distinction between two SOC gaps can be estimated utilizing the first-order SOC Hamiltonian $H_{soc}^{(1)} = \lambda L \cdot S$ (see [equation S27](#)),

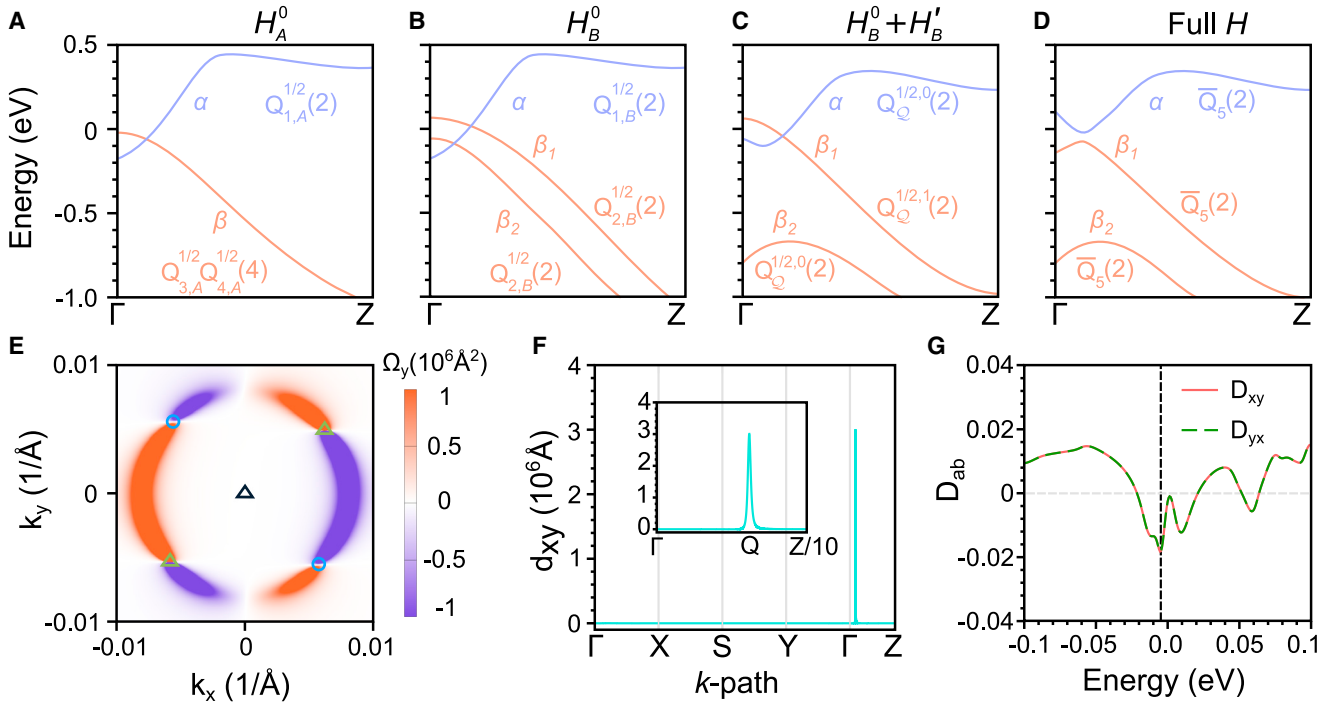


Figure 4. Quasi-symmetry and the nonlinear Hall effect in NdBiPt

(A–D) Evolution of bands α , β_1 , and β_2 for NdBiPt when considering different Hamiltonians: (A) the SOC-free Hamiltonian H_A^0 , (B) the Hamiltonian that includes diagonal first-order SOC terms $H_B^0 = H_A^0 + iL_zS_z$, (C) the Hamiltonian that includes off-diagonal first-order SOC term $H_B^0 + H'_B$, where $H'_B = \frac{i}{2}(L_+S_- + L_-S_+)$, and (D) the Hamiltonian H that considers the full SOC effects.

(E) Distribution of the Berry curvature within the $k_x - k_y$ plane.

(F) BCD density d_{xy} along the high-symmetry line. The inset denotes d_{xy} along the $\Gamma - Z/10$.

(G) Berry curvature dipole D_{ab} as a function of energy. The black dashed line represents the energy position of the Q point, which is 5.8 meV below the Fermi energy.

$$\Delta E_{\alpha\beta_1}^{(1)} \sim \langle \alpha | H_{\text{soc}}^{(1)} | \beta_1 \rangle = \lambda / 2(h_{15} + h_{25} + h_{16} + h_{26}) = 0 \text{ and} \quad (\text{Equation 2})$$

$$\Delta E_{\alpha\beta_2}^{(1)} \sim \langle \alpha | H_{\text{soc}}^{(1)} | \beta_2 \rangle = \lambda / 2(h_{13} + h_{23} + h_{14} + h_{24}) = \sqrt{2}\lambda / 2. \quad (\text{Equation 3})$$

Equations 2 and 3 show that the first-order SOC effect is prohibited for $\Delta E_{\alpha\beta_1}$, but allowed for $\Delta E_{\alpha\beta_2}$, consistent with the framework of quasi-symmetry analysis. Therefore, we demonstrate that the TCQ, two closely packed pairs of Weyl points within the tiny gap at the Q point, is protected by spin-orbit $U(1)$ quasi-symmetry.

DISCUSSION

The TCQ gathers the sources and sinks of Berry curvature in a very small region in momentum space, leading to a remarkable BCD. Thus, an enhanced nonlinear Hall effect is expected if the TCQ emerges around the Fermi level, as shown in Figure 1B. In $T\tau$ -AFM NdBiPt, there is only one independent element $D_{xy} = D_{yx}$ of the BCD tensor \mathbf{D} (see equation S2), where $D_{xy} = \int_{BZ} dk \sum_n f_0(\varepsilon_{nk}) \left(\frac{\partial}{\partial k_x} \Omega_y \right)$. The distribution of the Berry curvature Ω_y on the $k_x - k_y$ plane is shown in Figure 4E. We find

that Ω_y is mainly concentrated around the TCQ. Due to the presence of two glide mirrors $\{m_{100}|\tau\}$ and $\{m_{010}|\tau\}$, Ω_y is antisymmetric along the k_x direction and symmetric along the k_y direction. The gapped Q point (black triangles in Figure 4E) is located between the peaks of the positive and negative Berry curvature around the TCQ. Furthermore, the distribution of Ω_y in the vicinity of the Fermi surface is non-uniform due to the tilting of the Weyl cones. Overall, such a distribution pattern of the Berry curvature gives rise to a large BCD (see Figures S7 and S8).

The BCD density d_{xy} along the high-symmetry paths is shown in Figure 4F, indicating that the origin of d_{xy} comes entirely from the contribution of the TCQ around the Q point. Since the BCD is the integral of d_{xy} , it is consistent with our calculation, which shows that the BCD exhibits a peak at the position of the TCQ, as shown in Figure 4G. The large BCD value approaches 0.02 when the chemical potential is positioned at the TCQ (indicated by the black dashed line in Figure 4G). This value is comparable to the previous study on CuMnSb,⁴² where the BCD peak is located at about 100 meV above the Fermi level. In comparison, due to the clean Fermi surface composed of the TCQ, the BCD peak of NdBiPt is located only 5.8 meV below the Fermi level, making it favorable for experimental detection. Moreover, we expect that the TCQ can also be utilized to design a substantial circular photogalvanic effect, which shares close similarities to the BCD in terms of symmetry constraints.

In summary, based on the spin group analysis, we extend the quasi-symmetry theory to elucidate the formation of the TCQ quasiparticle, which is analogous to a charge quadrupole but composed of two closely packed pairs of Weyl points in momentum space. Our DFT calculations show that the non-centrosymmetric half-Heusler compound NdBiPt, with a collinear AFM configuration, is an ideal material candidate, manifesting a clean Fermi surface with TCQ. The structure of the TCQ is protected by mirror symmetry and, more importantly, the spin-orbit $U(1)$ quasi-symmetry, which eliminates the first-order SOC gap and leads to a significant nonlinear Hall effect induced by BCD. Overall, our research provides an avenue for designing unconventional quasiparticles through quasi-symmetries as well as material candidates with large nonlinear physical responses. Furthermore, the exotic transport properties induced by the TCQ can also facilitate the detection of the Néel vector, providing additional possibilities for AFM spintronics.

METHODS

The first-principles calculations utilized the projector augmented wave (PAW) method⁵³ within the Vienna Ab initio Simulation Package (VASP).⁵⁴ The exchange and correlation effects were treated by the generalized gradient approximation (GGA) with the Perdew-Burke-Ernzerhof (PBE) formalism.⁵⁵ An energy cutoff of 253 eV was employed for the calculations. The whole Brillouin zone was sampled by an $11 \times 11 \times 8$ Monkhorst-Pack grid⁵⁶ for all cells. Due to the local magnetic moments contributed by *f* electrons in Nd atoms, the GGA+*U* approach⁵⁷ within the Dudarev scheme⁵⁸ was applied. In our calculations, the TCQ of NdBiPt was relatively insensitive to the choice of U_{Nd} values (see Figure S9). For the convenience of discussion, we elaborated on the details using $U_{\text{Nd}} = 4$ eV as an example. A tight-binding Hamiltonian was obtained based on maximally localized Wannier functions of Nd *d* and *f* orbitals, Bi *p* orbitals, and Pt *s* and *d* orbitals. The maximally localized Wannier function was constructed using the WANNIER90 package,^{59,60} and the WannierTools package⁶¹ was utilized to calculate the surface states and the position of Weyl points. The WANNIERBERRI package⁶² was used to calculate the BCD, where a $500 \times 500 \times 500$ *k*-point mesh was used to achieve the convergence. The computation of the BCD is performed within the Fermi sea integral method, which is given as $D_{ab} = \int_{BZ} dk \sum f_0(\epsilon_{nk}) \left(\frac{\partial}{\partial k_a} \Omega_{nk}^b \right)$, where D_{ab} is the BCD, $f_0(\epsilon_{nk})$ is the Fermi-Dirac distribution, and Ω_{nk}^b denotes the Berry curvature. Further details regarding the methods can be found in the supplemental methods.

RESOURCE AVAILABILITY

Lead contact

Requests for additional information and resources should be directed to the lead contact, Qihang Liu (liuqh@sustech.edu.cn), who will address these inquiries.

Materials availability

This study did not generate new materials.

Data and code availability

All data needed to evaluate the conclusions in the paper are present in the paper and/or the [supplemental information](#). Additional data related to this paper may be requested from the authors.

ACKNOWLEDGMENTS

This work was supported by the National Key R&D Program of China under grant nos. 2019YFA0704900 and 2020YFA0308900, the National Natural Science Foundation of China under grant no. 12274194, the Guangdong Provincial Key Laboratory of Computational Science and Material Design under grant no. 2019B030301001, the Innovative Team of General Higher Educational Institutes in Guangdong Province (no. 2020KCXTD001), the Shenzhen Science and Technology Program (grant nos. RCJC20221008092722009 and 20231117091158001), and the Center for Computational Science and Engineering of Southern University of Science and Technology.

AUTHOR CONTRIBUTIONS

Q.L. conceived and designed the work. A.Z. and X.C. performed the calculations. A.Z., X.C., J.L., P.L., and Y.L. analyzed the results. A.Z., X.C., and Q.L. wrote the manuscript. All authors discussed the results and commented on the manuscript.

DECLARATION OF INTERESTS

The authors declare that they have no competing interests.

SUPPLEMENTAL INFORMATION

Supplemental information can be found online at <https://doi.org/10.1016/j.newton.2025.100010>.

Received: September 22, 2024

Revised: November 17, 2024

Accepted: January 7, 2025

Published: February 3, 2025

REFERENCES

1. Chiu, C.-K., Teo, J.C.Y., Schnyder, A.P., and Ryu, S. (2016). Classification of topological quantum matter with symmetries. Rev. Mod. Phys. 88, 035005. <https://doi.org/10.1103/RevModPhys.88.035005>.
2. Yan, B., and Felser, C. (2017). Topological Materials: Weyl Semimetals. Annu. Rev. Condens. Matter Phys. 8, 337–354. <https://doi.org/10.1146/annurev-conmatphys-031016-025458>.
3. Armitage, N.P., Mele, E.J., and Vishwanath, A. (2018). Weyl and Dirac semimetals in three-dimensional solids. Rev. Mod. Phys. 90, 015001. <https://doi.org/10.1103/RevModPhys.90.015001>.
4. Lv, B.Q., Qian, T., and Ding, H. (2021). Experimental perspective on three-dimensional topological semimetals. Rev. Mod. Phys. 93, 025002. <https://doi.org/10.1103/RevModPhys.93.025002>.
5. Wang, Z., Sun, Y., Chen, X.-Q., Franchini, C., Xu, G., Weng, H., Dai, X., and Fang, Z. (2012). Dirac semimetal and topological phase transitions in $A_3\text{Bi}$ ($A=\text{Na}, \text{K}, \text{Rb}$). Phys. Rev. B 85, 195320. <https://doi.org/10.1103/PhysRevB.85.195320>.
6. Young, S.M., Zaheer, S., Teo, J.C.Y., Kane, C.L., Mele, E.J., and Rappe, A.M. (2012). Dirac Semimetal in Three Dimensions. Phys. Rev. Lett. 108, 140405. <https://doi.org/10.1103/PhysRevLett.108.140405>.
7. Wang, Z., Weng, H., Wu, Q., Dai, X., and Fang, Z. (2013). Three-dimensional Dirac semimetal and quantum transport in Cd_3As_2 . Phys. Rev. B 88, 125427. <https://doi.org/10.1103/PhysRevB.88.125427>.
8. Liu, Z.K., Jiang, J., Zhou, B., Wang, Z.J., Zhang, Y., Weng, H.M., Prabhakaran, D., Mo, S.K., Peng, H., Dudin, P., et al. (2014). A stable

- three-dimensional topological Dirac semimetal Cd_3As_2 . *Nat. Mater.* 13, 677–681. <https://doi.org/10.1038/nmat3990>.
9. Liu, Z.K., Zhou, B., Zhang, Y., Wang, Z.J., Weng, H.M., Prabhakaran, D., Mo, S.-K., Shen, Z.X., Fang, Z., Dai, X., et al. (2014). Discovery of a Three-Dimensional Topological Dirac Semimetal, Na_3Bi . *Science* 343, 864–867. <https://doi.org/10.1126/science.1245085>.
10. Xu, S.-Y., Liu, C., Kushwaha, S.K., Sankar, R., Krizan, J.W., Belopolski, I., Neupane, M., Bian, G., Alidoust, N., Chang, T.-R., et al. (2015). Observation of Fermi arc surface states in a topological metal. *Science* 347, 294–298. <https://doi.org/10.1126/science.1256742>.
11. Wan, X., Turner, A.M., Vishwanath, A., and Savrasov, S.Y. (2011). Topological semimetal and Fermi-arc surface states in the electronic structure of pyrochlore iridates. *Phys. Rev. B* 83, 205101. <https://doi.org/10.1103/PhysRevB.83.205101>.
12. Weng, H., Fang, C., Fang, Z., Bernevig, B.A., and Dai, X. (2015). Weyl Semimetal Phase in Noncentrosymmetric Transition-Metal Monophosphides. *Phys. Rev. X* 5, 011029. <https://doi.org/10.1103/PhysRevX.5.011029>.
13. Huang, S.-M., Xu, S.-Y., Belopolski, I., Lee, C.-C., Chang, G., Wang, B., Alidoust, N., Bian, G., Neupane, M., Zhang, C., et al. (2015). A Weyl Fermion semimetal with surface Fermi arcs in the transition metal monopnictide $TaAs$ class. *Nat. Commun.* 6, 7373. <https://doi.org/10.1038/ncomms8373>.
14. Xu, S.-Y., Belopolski, I., Alidoust, N., Neupane, M., Bian, G., Zhang, C., Sankar, R., Chang, G., Yuan, Z., Lee, C.-C., et al. (2015). Discovery of a Weyl fermion semimetal and topological Fermi arcs. *Science* 349, 613–617. <https://doi.org/10.1126/science.aaa9297>.
15. Lv, B.Q., Weng, H.M., Fu, B.B., Wang, X.P., Miao, H., Ma, J., Richard, P., Huang, X.C., Zhao, L.X., Chen, G.F., et al. (2015). Experimental Discovery of Weyl Semimetal $TaAs$. *Phys. Rev. X* 5, 031013. <https://doi.org/10.1103/PhysRevX.5.031013>.
16. Yang, L.X., Liu, Z.K., Sun, Y., Peng, H., Yang, H.F., Zhang, T., Zhou, B., Zhang, Y., Guo, Y.F., Rahn, M., et al. (2015). Weyl semimetal phase in the non-centrosymmetric compound $TaAs$. *Nat. Phys.* 11, 728–732. <https://doi.org/10.1038/nphys3425>.
17. Lv, B.Q., Xu, N., Weng, H.M., Ma, J.Z., Richard, P., Huang, X.C., Zhao, L.X., Chen, G.F., Matt, C.E., Bisti, F., et al. (2015). Observation of Weyl nodes in $TaAs$. *Nat. Phys.* 11, 724–727. <https://doi.org/10.1038/nphys3426>.
18. Sun, Y., Wu, S.-C., and Yan, B. (2015). Topological surface states and Fermi arcs of the noncentrosymmetric Weyl semimetals $TaAs$, TaP , $NbAs$, and NbP . *Phys. Rev. B* 92, 115428. <https://doi.org/10.1103/PhysRevB.92.115428>.
19. Liu, Z.K., Yang, L.X., Sun, Y., Zhang, T., Peng, H., Yang, H.F., Chen, C., Zhang, Y., Guo, Y.F., Prabhakaran, D., et al. (2016). Evolution of the Fermi surface of Weyl semimetals in the transition metal pnictide family. *Nat. Mater.* 15, 27–31. <https://doi.org/10.1038/nmat4457>.
20. Bradlyn, B., Cano, J., Wang, Z., Vergniory, M.G., Felser, C., Cava, R.J., and Bernevig, B.A. (2016). Beyond Dirac and Weyl fermions: Unconventional quasiparticles in conventional crystals. *Science* 353, aaf5037. <https://doi.org/10.1126/science.aaf5037>.
21. Lv, B.Q., Feng, Z.L., Xu, Q.N., Gao, X., Ma, J.Z., Kong, L.Y., Richard, P., Huang, Y.B., Strocov, V.N., Fang, C., et al. (2017). Observation of three-component fermions in the topological semimetal molybdenum phosphide. *Nature* 546, 627–631. <https://doi.org/10.1038/nature22390>.
22. Ma, J.Z., He, J.B., Xu, Y.F., Lv, B.Q., Chen, D., Zhu, W.L., Zhang, S., Kong, L.Y., Gao, X., Rong, L.Y., et al. (2018). Three-component fermions with surface Fermi arcs in tungsten carbide. *Nat. Phys.* 14, 349–354. <https://doi.org/10.1038/s41567-017-0021-8>.
23. Yu, Z.-M., Zhang, Z., Liu, G.-B., Wu, W., Li, X.-P., Zhang, R.-W., Yang, S.A., and Yao, Y. (2022). Encyclopedia of emergent particles in three-dimensional crystals. *Sci. Bull.* 67, 375–380. <https://doi.org/10.1016/scib.2021.10.023>.
24. Slager, R.-J., Mesaros, A., Juričić, V., and Zaanen, J. (2013). The space group classification of topological band-insulators. *Nat. Phys.* 9, 98–102. <https://doi.org/10.1038/nphys2513>.
25. Kruthoff, J., de Boer, J., van Wezel, J., Kane, C.L., and Slager, R.-J. (2017). Topological Classification of Crystalline Insulators through Band Structure Combinatorics. *Phys. Rev. X* 7, 041069. <https://doi.org/10.1103/PhysRevX.7.041069>.
26. Watanabe, H., Po, H.C., and Vishwanath, A. (2018). Structure and topology of band structures in the 1651 magnetic space groups. *Sci. Adv.* 4, eaat8685. <https://doi.org/10.1126/sciadv.aat8685>.
27. Zhang, T., Jiang, Y., Song, Z., Huang, H., He, Y., Fang, Z., Weng, H., and Fang, C. (2019). Catalogue of topological electronic materials. *Nature* 566, 475–479. <https://doi.org/10.1038/s41586-019-0944-6>.
28. Tang, F., Po, H.C., Vishwanath, A., and Wan, X. (2019). Comprehensive search for topological materials using symmetry indicators. *Nature* 566, 486–489. <https://doi.org/10.1038/s41586-019-0937-5>.
29. Vergniory, M.G., Elcoro, L., Felser, C., Regnault, N., Bernevig, B.A., and Wang, Z. (2019). A complete catalogue of high-quality topological materials. *Nature* 566, 480–485. <https://doi.org/10.1038/s41586-019-0954-4>.
30. Xu, Y., Elcoro, L., Song, Z.-D., Wieder, B.J., Vergniory, M.G., Regnault, N., Chen, Y., Felser, C., and Bernevig, B.A. (2020). High-throughput calculations of magnetic topological materials. *Nature* 586, 702–707. <https://doi.org/10.1038/s41586-020-2837-0>.
31. Bouhon, A., Lange, G.F., and Slager, R.-J. (2021). Topological correspondence between magnetic space group representations and subdimensions. *Phys. Rev. B* 103, 245127. <https://doi.org/10.1103/PhysRevB.103.245127>.
32. Elcoro, L., Wieder, B.J., Song, Z., Xu, Y., Bradlyn, B., and Bernevig, B.A. (2021). Magnetic topological quantum chemistry. *Nat. Commun.* 12, 5965. <https://doi.org/10.1038/s41467-021-26241-8>.
33. Peng, B., Jiang, Y., Fang, Z., Weng, H., and Fang, C. (2022). Topological classification and diagnosis in magnetically ordered electronic materials. *Phys. Rev. B* 105, 235138. <https://doi.org/10.1103/PhysRevB.105.235138>.
34. Yang, J., Liu, Z.-X., and Fang, C. (2021). Symmetry invariants and classes of quasi-particles in magnetically ordered systems having weak spin-orbit coupling. Preprint at arXiv. <https://doi.org/10.48550/arXiv.2105.12738>.
35. Guo, P.-J., Wei, Y.-W., Liu, K., Liu, Z.-X., and Lu, Z.-Y. (2021). Eightfold Degenerate Fermions in Two Dimensions. *Phys. Rev. Lett.* 127, 176401. <https://doi.org/10.1103/PhysRevLett.127.176401>.
36. Liu, P., Li, J., Han, J., Wan, X., and Liu, Q. (2022). Spin-Group Symmetry in Magnetic Materials with Negligible Spin-Orbit Coupling. *Phys. Rev. X* 12, 021016. <https://doi.org/10.1103/PhysRevX.12.021016>.
37. Liu, P., Zhang, A., Han, J., and Liu, Q. (2022). Chiral Dirac-like fermion in spin-orbit-free antiferromagnetic semimetals. *Innovations* 3, 100343. <https://doi.org/10.1016/j.xinn.2022.100343>.
38. Zhang, A., Deng, K., Sheng, J., Liu, P., Kumar, S., Shimada, K., Jiang, Z., Liu, Z., Shen, D., and Li, J. (2023). Chiral Dirac fermion in a collinear antiferromagnet. *Chin. Phys. Lett.* 40, 126101. <https://doi.org/10.1088/0256-307X/40/12/126101>.
39. Chen, X., Liu, Y., Liu, P., Yu, Y., Ren, J., Li, J., Zhang, A., and Liu, Q. (2023). Catalog of Unconventional Magnons in Collinear Magnets. Preprint at arXiv. <https://doi.org/10.48550/arXiv.2307.12366>.
40. Liu, E., Sun, Y., Kumar, N., Müchler, L., Sun, A., Jiao, L., Yang, S.-Y., Liu, D., Liang, A., Xu, Q., et al. (2018). Giant anomalous Hall effect in a ferromagnetic kagome-lattice semimetal. *Nat. Phys.* 14, 1125–1131. <https://doi.org/10.1038/s41567-018-0234-5>.
41. Wang, Q., Xu, Y., Lou, R., Liu, Z., Li, M., Huang, Y., Shen, D., Weng, H., Wang, S., and Lei, H. (2018). Large intrinsic anomalous Hall effect in half-metallic ferromagnet $Co_3Sn_2S_2$ with magnetic Weyl fermions. *Nat. Commun.* 9, 3681. <https://doi.org/10.1038/s41467-018-06088-2>.
42. Shao, D.F., Zhang, S.H., Gurung, G., Yang, W., and Tsymbal, E.Y. (2020). Nonlinear Anomalous Hall Effect for Néel Vector Detection. *Phys. Rev. Lett.* 124, 067203. <https://doi.org/10.1103/PhysRevLett.124.067203>.

43. Guo, C., Hu, L., Putzke, C., Diaz, J., Huang, X., Manna, K., Fan, F.-R., Shekhar, C., Sun, Y., Felser, C., et al. (2022). Quasi-symmetry-protected topology in a semi-metal. *Nat. Phys.* **18**, 813–818. <https://doi.org/10.1038/s41567-022-01604-0>.
44. Li, J., Zhang, A., Liu, Y., and Liu, Q. (2024). Group Theory on Quasisymmetry and Protected Near Degeneracy. *Phys. Rev. Lett.* **133**, 026402. <https://doi.org/10.1103/PhysRevLett.133.026402>.
45. You, J.-S., Fang, S., Xu, S.-Y., Kaxiras, E., and Low, T. (2018). Berry curvature dipole current in the transition metal dichalcogenides family. *Phys. Rev. B* **98**, 121109. <https://doi.org/10.1103/PhysRevB.98.121109>.
46. Müller, R.A., Desilets-Benoit, A., Gauthier, N., Lapointe, L., Bianchi, A.D., Maris, T., Zahn, R., Beyer, R., Green, E., Wosnitza, J., et al. (2015). Magnetic structure of the antiferromagnetic half-Heusler compound NdBiPt. *Phys. Rev. B* **92**, 184432. <https://doi.org/10.1103/PhysRevB.92.184432>.
47. Chen, X., Ren, J., Zhu, Y., Yu, Y., Zhang, A., Liu, P., Li, J., Liu, Y., Li, C., and Liu, Q. (2024). Enumeration and Representation Theory of Spin Space Groups. *Phys. Rev. X* **14**, 031038. <https://doi.org/10.1103/PhysRevX.14.031038>.
48. <https://findspingroup.com>.
49. Liu, L., Liu, Y., Li, J., Wu, H., and Liu, Q. (2024). Quantum spin Hall effect protected by spin $U(1)$ quasisymmetry. *Phys. Rev. B* **110**, L161104. <https://doi.org/10.1103/PhysRevB.110.L161104>.
50. Kitamura, S., Usui, H., Slager, R.-J., Bouhon, A., Sunko, V., Rosner, H., King, P.D., Orenstein, J., Moessner, R., and Mackenzie, A.P. (2018). Spin Hall effect in 2D metallic delafossite PtCoO_2 and vicinity topology. Preprint at arXiv. <https://doi.org/10.48550/arXiv.1811.03105>.
51. Sun, F., Ye, J., and Liu, W.-M. (2015). Quantum magnetism of spinor bosons in optical lattices with synthetic non-Abelian gauge fields. *Phys. Rev.* **92**, 043609. <https://doi.org/10.1103/PhysRevA.92.043609>.
52. Lee, J.Y., Khalaf, E., Liu, S., Liu, X., Hao, Z., Kim, P., and Vishwanath, A. (2019). Theory of correlated insulating behaviour and spin-triplet superconductivity in twisted double bilayer graphene. *Nat. Commun.* **10**, 5333. <https://doi.org/10.1038/s41467-019-12981-1>.
53. Kresse, G., and Joubert, D. (1999). From ultrasoft pseudopotentials to the projector augmented-wave method. *Phys. Rev. B* **59**, 1758–1775. <https://doi.org/10.1103/PhysRevB.59.1758>.
54. Kresse, G., and Furthmüller, J. (1996). Efficient iterative schemes for ab initio total-energy calculations using a plane-wave basis set. *Phys. Rev. B* **54**, 11169–11186. <https://doi.org/10.1103/PhysRevB.54.11169>.
55. Perdew, J.P., Burke, K., and Ernzerhof, M. (1996). Generalized Gradient Approximation Made Simple. *Phys. Rev. Lett.* **77**, 3865–3868. <https://doi.org/10.1103/PhysRevLett.77.3865>.
56. Monkhorst, H.J., and Pack, J.D. (1976). Special Points for Brillouin-Zone Integrations. *Phys. Rev. B* **13**, 5188–5192. <https://doi.org/10.1103/PhysRevB.13.5188>.
57. Liechtenstein, A.I., Anisimov, V.I., and Zaanen, J. (1995). Density-Functional Theory and Strong-Interactions - Orbital Ordering in Mott-Hubbard Insulators. *Phys. Rev. B* **52**, R5467–R5470. <https://doi.org/10.1103/PhysRevB.52.R5467>.
58. Dudarev, S.L., Botton, G.A., Savrasov, S.Y., Humphreys, C.J., and Sutton, A.P. (1998). Electron-energy-loss spectra and the structural stability of nickel oxide: An LSDA+U study. *Phys. Rev. B* **57**, 1505–1509. <https://doi.org/10.1103/PhysRevB.57.1505>.
59. Mostofi, A.A., Yates, J.R., Lee, Y.S., Souza, I., Vanderbilt, D., and Marzari, N. (2008). wannier90: A tool for obtaining maximally-localised Wannier functions. *Comput. Phys. Commun.* **178**, 685–699. <https://doi.org/10.1016/j.cpc.2007.11.016>.
60. Marzari, N., Mostofi, A.A., Yates, J.R., Souza, I., and Vanderbilt, D. (2012). Maximally localized Wannier functions: Theory and applications. *Rev. Mod. Phys.* **84**, 1419–1475. <https://doi.org/10.1103/RevModPhys.84.1419>.
61. Wu, Q., Zhang, S., Song, H.F., Troyer, M., and Soluyanov, A.A. (2018). WannierTools: An open-source software package for novel topological materials. *Comput. Phys. Commun.* **224**, 405–416. <https://doi.org/10.1016/j.cpc.2017.09.033>.
62. Tsirkin, S.S. (2021). High performance Wannier interpolation of Berry curvature and related quantities with WannierBerri code. *npj Comput. Mater.* **7**, 33. <https://doi.org/10.1038/s41524-021-00498-5>.

NEWTON, Volume 1

Supplemental information

**Topological charge quadrupole protected
by spin-orbit $U(1)$ quasi-symmetry
in antiferromagnet NdBiPt**

Ao Zhang, Xiaobing Chen, Jiayu Li, Pengfei Liu, Yuntian Liu, and Qihang Liu

Supplemental Methods

A. Symmetry analysis and electronic structure of NdBiPt

The elements of the magnetic space group and the spin space group for NdBiPt are listed in Table S1. In the presence of SOC, all bands along $\Gamma - Z$ are twofold degenerate. This is protected by the magnetic little co-group $\bar{4}'m2'$. Specifically, a two-fold rotation $C_{2z} = \{2_{001}|0\}$ and a glide mirror operation $g_{010} = \{m_{010}|1/2, 1/2, 1/2\}$ in this group could account for the degeneracy. Since $(C_{2z})^2 = -1$, eigenvalues of C_{2z} are $\pm i$. Meanwhile, g_{010} and C_{2z} satisfy the anticommutation relation because spin rotations in these two operations anticommute with one another. These two conditions imply that every eigenstate of C_{2z} could be connected to another eigenstate with an opposite eigenvalue by the operation g_{010} , forcing them to degenerate along the $\Gamma - Z$ line (Obviously, two states with different symmetry eigenvalues are orthogonal).

We next investigate the symmetry constraints on the Berry curvature dipole \mathbf{D} can be expressed as follows,

$$\mathbf{D} = \det(\widehat{O})\widehat{O}\mathbf{D}\widehat{O}^T, \quad (\text{Equation S1})$$

where \widehat{O} is a symmetry operation included in the point group. For NdBiPt, the magnetic space group is $P_1\bar{4}n2$ (No. 118.314), with the corresponding magnetic point group being $\bar{4}m2.1'$, and the generators of $\bar{4}m2.1'$ are $\bar{4}_{001}$, m_{100} , 2_{110} , and $1'$. By applying these generators to berry curvature dipole \mathbf{D} according to Eq. (S1), we obtain,

$$\mathbf{D} = \begin{bmatrix} D_{xx} & D_{xy} & D_{xz} \\ D_{yx} & D_{yy} & D_{yz} \\ D_{zx} & D_{zy} & D_{zz} \end{bmatrix} = \begin{bmatrix} 0 & D_{xy} & 0 \\ D_{xy} & 0 & 0 \\ 0 & 0 & 0 \end{bmatrix}. \quad (\text{Equation S2})$$

Consequently, we confirm that $D_{xy} = D_{yx}$.

Table S1. Group elements of the magnetic space group and spin group describing collinear AFM NdBiPt. The spin space group $P^1\bar{4}^1m^12^{-1}(1/2\ 1/2\ 1/2)^{\infty m1}$ can be generated from the direct product of the nontrivial spin space group and the spin-only group as tabulated in Table S1, respectively. Here $\{m||1|0\} = TU_n(\pi) = TU$, $\{\infty||1|0\} = U_z(\theta)$ represent the mirror symmetry and the continuous spin rotations along the collinear spin axis in spin space, respectively.

	Group elements
Magnetic space group $P_1\bar{4}n2$ (No. 118.314)	$\{1 0\}, \{2_{001} 0\}, \{2_{001} 1/2, 1/2, 1/2\}, \{2_{1\bar{1}0} 1/2, 1/2, 1/2\}, \{\bar{4}_{001}^+ 0\}, \{\bar{4}_{001}^- 0\}, \{m_{100} 1/2, 1/2, 1/2\}, \{m_{010} 1/2, 1/2, 1/2\}, \{1' 1/2, 1/2, 1/2\}, \{2_{001}^+ 1/2, 1/2, 1/2\}, \{2_{110}^+ 0\}, \{2_{1\bar{1}0}^+ 0\}, \{\bar{4}_{001}^+ 1/2, 1/2, 1/2\}, \{\bar{4}_{001}^- 1/2, 1/2, 1/2\}, \{m_{100} 0\}, \{m_{010} 0\}$
Spin space group $P^1\bar{4}^1m^12^{-1}(1/2\ 1/2\ 1/2)^{\infty m1}$ (No. 115.119.2.1)	Nontrivial spin space group: $\{1 1 0\}, \{1 2_{001} 0\}, \{1 2_{110} 0\}, \{1 2_{1\bar{1}0} 0\}, \{1 \bar{4}_{001}^+ 0\}, \{1 \bar{4}_{001}^- 0\}, \{1 m_{100} 0\}, \{1 m_{010} 0\}, \{\bar{1} 1 1/2, 1/2, 1/2\}, \{\bar{1} 2_{001} 1/2, 1/2, 1/2\},$

	$\{\bar{1} 2_{110} 1/2,1/2,1/2\}$, $\{\bar{1} 2_{1\bar{1}0} 1/2,1/2,1/2\}$, $\{\bar{1} \bar{4}_{001}^+ 1/2,1/2,1/2\}$, $\{\bar{1} \bar{4}_{001}^- 1/2,1/2,1/2\}$, $\{\bar{1} m_{100} 1/2,1/2,1/2\}$, $\{\bar{1} m_{010} 1/2,1/2,1/2\}$, Spin-only group (only generators): $\{m 1 0\}$, $\{\infty 1 0\}$
--	---

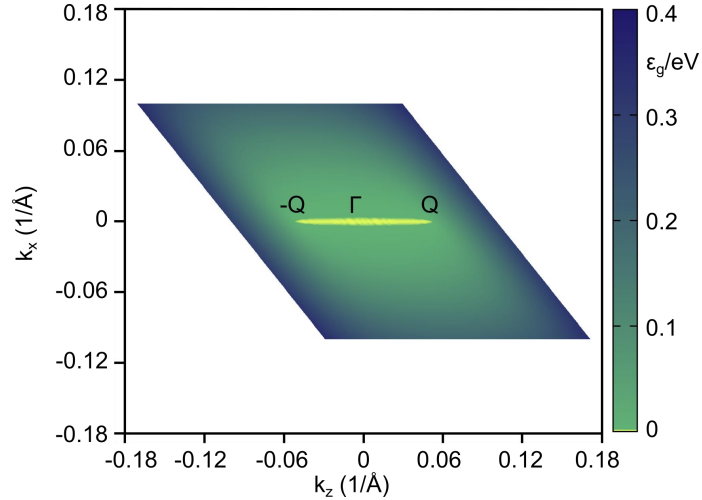


Fig. S1. Inverse gap ε_g as a function of k_z and k_x without spin-orbit coupling. The position with a gap of zero is marked with a yellow-green color. The Dirac nodal line is along the $-Q - \Gamma - Q$ on the $k_z - k_x$ plane.

We investigated the effect of spin-orbit coupling (SOC) on the electronic structure of NdBiPt by artificially varying λ , where λ denotes the overall SOC strength of NdBiPt. After considering the SOC, the bands highlighted by the black dashed arrows undergo a downward shift as the strength of the SOC increases (as shown in Figs. S2a-f). When the $\lambda = 1$ (as shown in Fig. S2f), a Rashba-like band structure emerges at the Γ point.

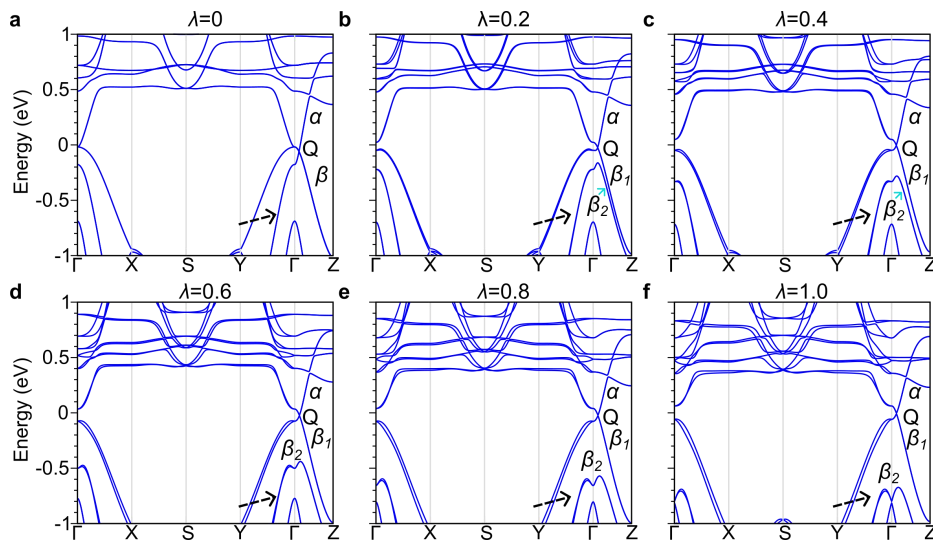


Fig. S2. The band structures of NdBiPt with different SOC strength λ . The Fermi level is set to zero.

For the distribution of Weyl points in the Brillouin zone of NdBiPt (see Fig. 3a of the main text), the distance between the nearest neighboring Weyl points near the $\pm Q$ point is exceedingly small, approximately 0.01 \AA^{-1} , corresponding to $1/131$ of the in-plane lattice parameter of the first Brillouin zone. Moreover, the Chern numbers of nearest neighboring Weyl points are opposite near $Q/-Q$ point, which is protected by two glide mirror symmetries, $\{m_{100}|1/2, 1/2, 1/2\}$ and $\{m_{010}|1/2, 1/2, 1/2\}$ (see Fig. S3 and Table S1). Therefore, two pairs of Weyl points near the $Q/-Q$ point can be viewed as a topological charge quadrupole.

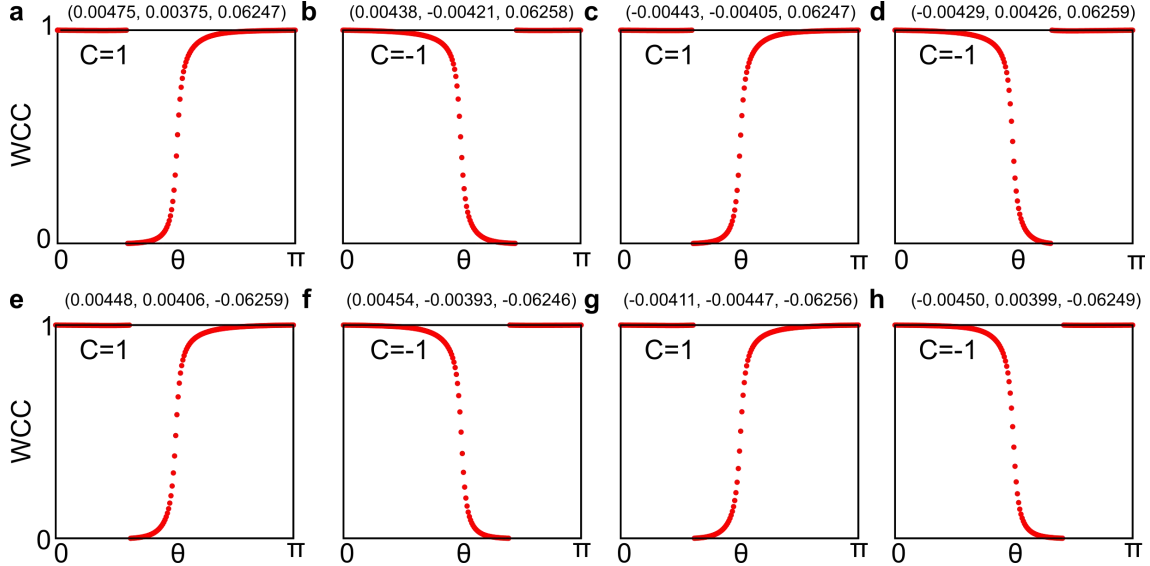


Fig. S3. The Wannier charge centers (WCCs) and the Chern numbers of eight Weyl points. a-d and e-h denote the WCCs of the Weyl points near the Q and $-Q$ points, respectively. The coordinates of the Weyl point are marked at the top of the figure. The computational precision introduces deviations in the coordinates of Weyl points constrained by symmetry.

We next focus on the α and β bands along the $\Gamma - Z$ path (see Fig. S2a). Without considering the SOC effect, the α band displays a double degeneracy, while the β band exhibits a quadruple degeneracy (see Fig. 2c of main text). When considering the SOC effect, a branch of the β band shifts downwards as indicated by the black dashed arrows in Fig. S2, resulting in the splitting of the β band into two sub-bands, β_1 and β_2 , both showing a double degeneracy. We conducted an orbital analysis using the band structure with $\lambda = 0.2$ (see Fig. S2b) as an example. Upon analyzing the orbital-projected band structure, it is observed that the α band is predominantly contributed by the s orbital of Nd, and the s and p_z orbitals of Bi and Pt atoms (see Figs. S4-S6). Additionally, the β_1 and β_2 bands are mainly influenced by the d_{xz} and d_{yz} orbitals of Nd, and the p_x , p_y , d_{xz} , and d_{yz} orbitals of Bi and Pt atoms (see Figs. S4-S6).

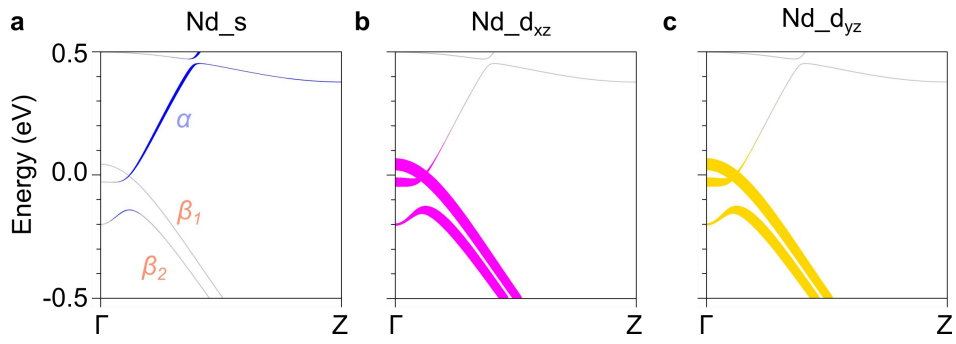


Fig. S4. Orbital-projected band structures weighted by atomic orbitals of Nd.

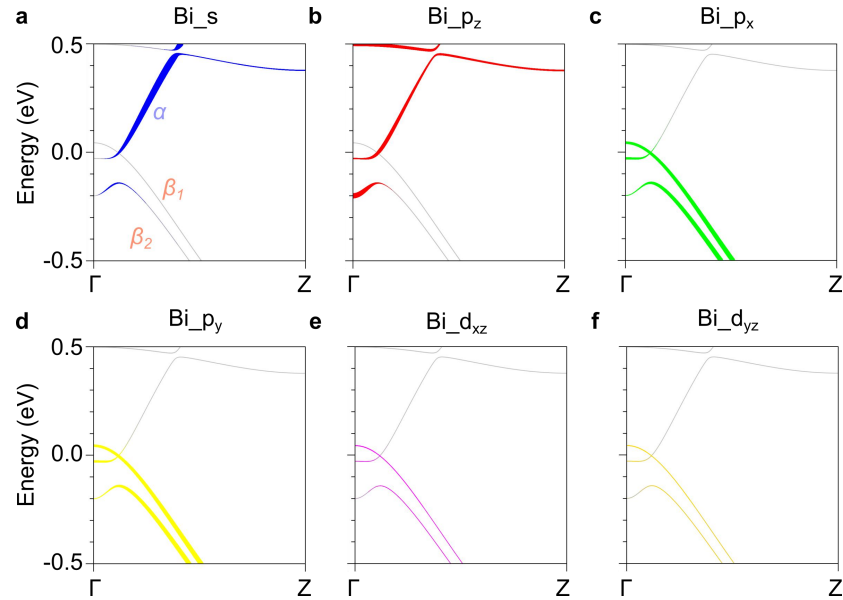


Fig. S5. Orbital-projected band structures weighted by atomic orbitals of Bi.

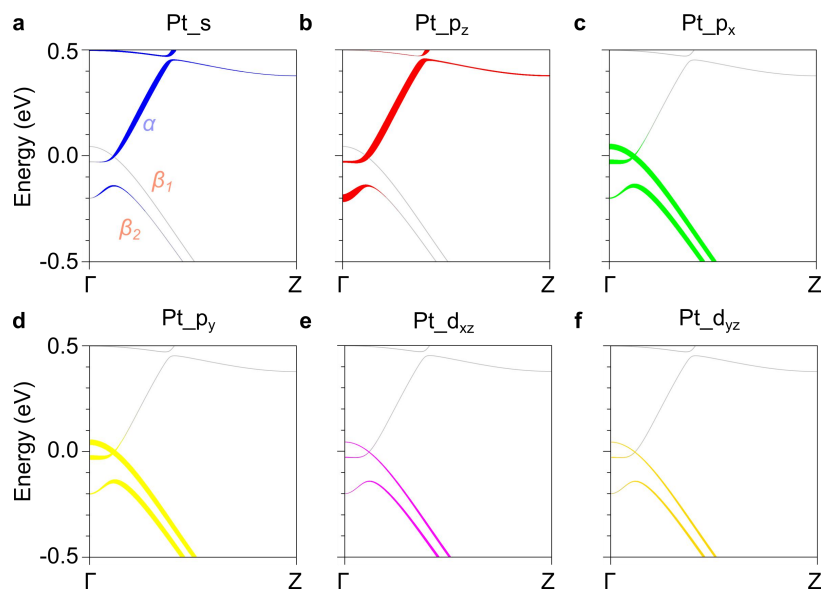


Fig. S6. Orbital-projected band structures weighted by atomic orbitals of Pt.

Table S2. The dominant orbital contributions of the α , β_1 , and β_2 bands.

	Nd	Bi	Pt
α	s	s, p_z	s, p_z
β_1/β_2	d_{xz}, d_{yz}	p_x, p_y, d_{xz}, d_{yz}	p_x, p_y, d_{xz}, d_{yz}

The non-uniform distribution of Berry curvature Ω_y near the topological charge quadrupole results in the emergence of a Berry curvature dipole D_{xy} for NdBiPt. Specifically, due to the presence of two glide mirrors $\{m_{100}|1/2, 1/2, 1/2\}$ and $\{m_{010}|1/2, 1/2, 1/2\}$, we have $\Omega_y(A) = \Omega_y(G) = -\Omega_y(C) = -\Omega_y(H)$ and $\Omega_y(B) = \Omega_y(E) = -\Omega_y(D) = -\Omega_y(F)$ as shown in Fig. S7b. However, the absence of symmetry establishes a connection between the points within the topological charge quadrupole (points B, E, D, and F) and its external points (points A, G, C, and H). Therefore, these Weyl cones inevitably tilt. Moreover, our first-principles calculations also confirm that the Weyl points constituting the topological charge quadrupole in NdBiPt exhibit tilt along the k_x and k_y directions (see Fig. S8). Therefore, these tilted Weyl cone leads to a non-uniform distribution of Berry curvature Ω_y on the Fermi surface (see Fig. S7c), resulting in the formation of Berry curvature dipoles D_{xy} .

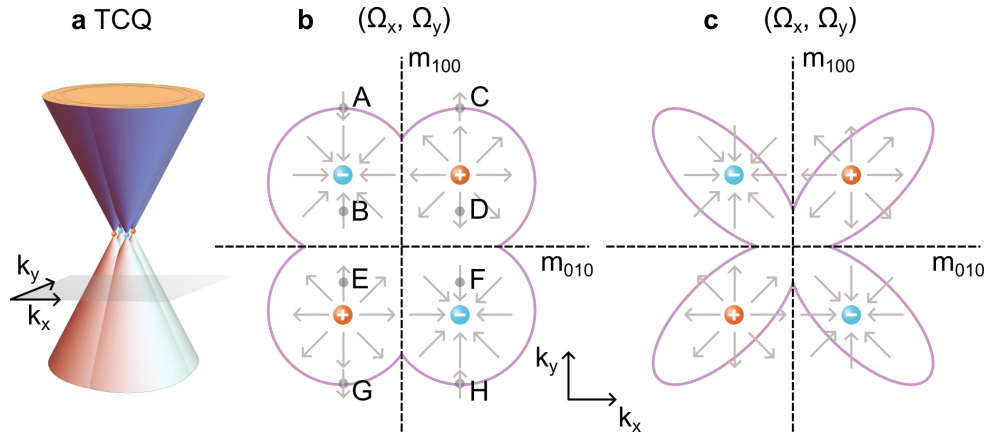


Fig. S7. a Schematic representation of the band structures of the topological charge quadrupole (TCQ). **b** and **c** represent the Berry curvature and the Fermi surface of the TCQ formed by the untilted and tilted Weyl points, respectively.

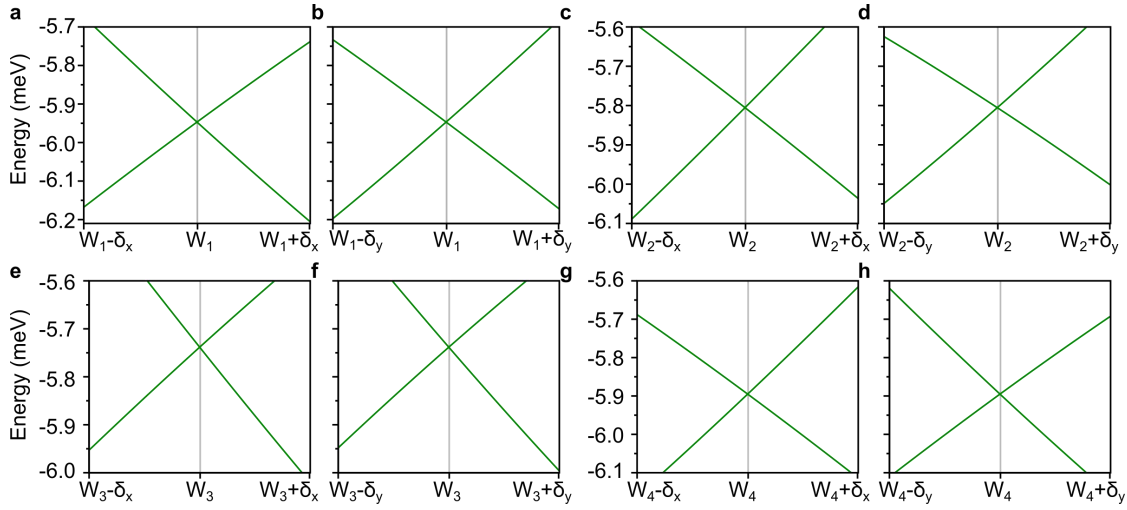


Fig. S8. The electronic structures of Weyl points near the Q point, where $W_1 = (-0.00429, 0.00426, 0.06259)$, $W_2 = (0.00475, 0.00375, 0.06247)$, $W_3 = (-0.00443, -0.00405, 0.06247)$, $W_4 = (0.00438, -0.00421, 0.06258)$, $\delta_x = (0.0005, 0, 0)$, and $\delta_y = (0, 0.0005, 0)$.

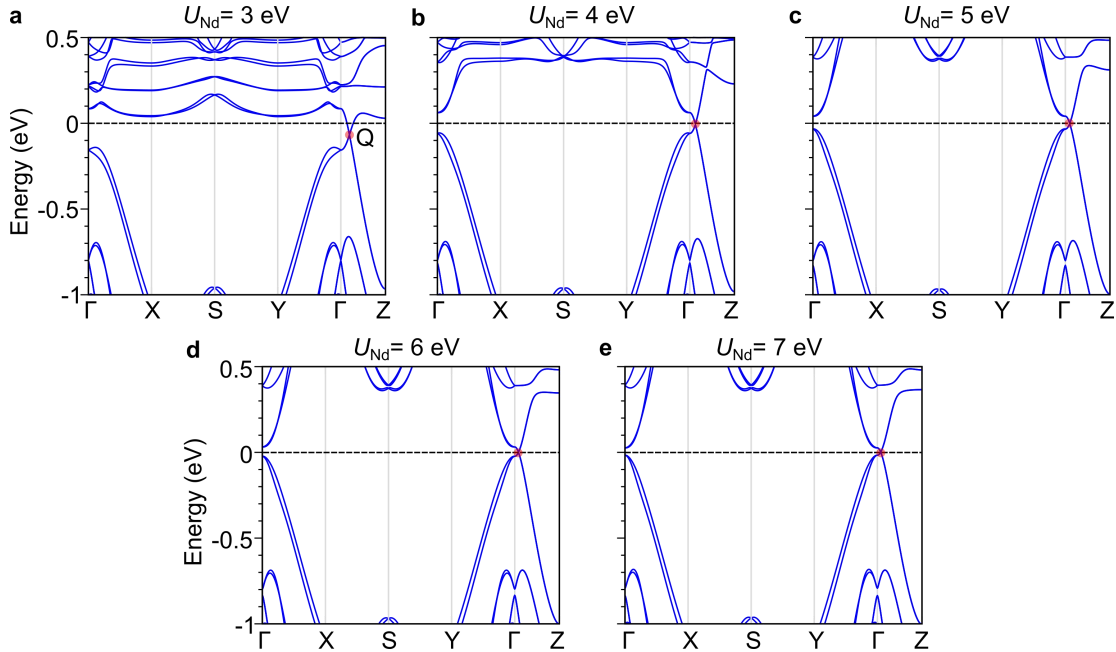


Fig. S9. Electronic structures with varying U_{Nd} values for NdBiPt. a-e The band structures of NdBiPt for selected U_{Nd} values (3, 4, 5, 6, 7 eV). The black dashed lines denote the Fermi levels. Pink circles indicate the positions of the Q points.

B. Failure of traditional approach towards partially lifted degeneracy

In the absence of SOC, the symmetry of the single-electron Hamiltonian $H_A^0 = H_k + H_p + H_{mag}$, which includes the kinetic term H_k , the potential term H_p and the magnetic term H_{mag} , can be

described by the collinear spin space group $G_{H_A^0} = G_S = P^{\frac{1}{4}} \bar{1} m^1 2^{-1} (1/2\ 1/2\ 1/2)^{\circ m} 1$. The character table of the little group $G_{H_A^0}^Q = {}^m \bar{4}^1 m^m 2^{\circ m} 1$ is given in Table S3, where the doubly degenerate band α and the quadruply degenerate band β correspond to irreps $Q_{1,A}^{1/2}(2)$ and $Q_{3,A}^{1/2} Q_{4,A}^{1/2}(4)$, respectively.

We first consider the selection rule of band splitting when considering the perturbed term $H'_A = H_{soc}^{(1)} = \lambda L \cdot S = \lambda L_z S_z + \frac{\lambda}{2} (L_+ S_- + L_- S_+)$. In the little group of $G_{H_A^0}^Q$, we can find that $\langle \alpha | L_z S_z | \beta \rangle$ is $G_{H_A^0}^Q$ -forbidden while $\langle \alpha | L_+ S_- + L_- S_+ | \beta \rangle$ is $G_{H_A^0}^Q$ -allowed splitting, as given in Eq. (S3) and Eq. (S4), respectively.

$$\begin{aligned} \langle \alpha | L_z S_z | \beta \rangle &\sim Q_{1,A}^{1/2} \otimes Q_{2,A}^{0-} \otimes Q_{3,A}^{1/2} Q_{4,A}^{1/2} \\ &= Q_{3,A}^{0+} Q_{4,A}^{0+} + Q_{3,A}^{0-} Q_{4,A}^{0-} + Q_{3,A}^1 Q_{4,A}^1 \end{aligned} \quad (\text{Equation S3})$$

$$\begin{aligned} \langle \alpha | L_+ S_- + L_- S_+ | \beta \rangle &\sim Q_{1,A}^{1/2} \otimes (Q_{3,A}^{0+} Q_{4,A}^{0+} + Q_{3,A}^{0-} Q_{4,A}^{0-}) \otimes Q_{3,A}^{1/2} Q_{4,A}^{1/2} \\ &= 4Q_{1,A}^{0+} + 4Q_{2,A}^{0+} + 4Q_{1,A}^{0-} + 4Q_{2,A}^{0-} + 4Q_{1,A}^1 + 4Q_{2,A}^1 \end{aligned} \quad (\text{Equation S4})$$

Table S3. Character table of the little group $G_{H_A^0}^Q = {}^m \bar{4}^1 m^m 2^{\circ m} 1$, where $\omega_S = \cos m_S \theta$, m_S is the spin angular momentum. Only unitary group elements are shown here.

	$Q_{1,A}^{0+}$	$Q_{2,A}^{0+}$	$Q_{3,A}^{0+} Q_{4,A}^{0+}$	$Q_{1,A}^{0-}$	$Q_{2,A}^{0-}$	$Q_{3,A}^{0-} Q_{4,A}^{0-}$	$Q_{1,A}^{m_S}$	$Q_{2,A}^{m_S}$	$Q_{3,A}^{m_S} Q_{4,A}^{m_S}$
{1 1 0}	1	1	2	1	1	2	2	2	4
{1 2 ₀₀₁ 0}	1	1	-2	1	1	-2	2	2	-4
{1 m ₀₁₀ 0}	1	-1	0	1	-1	0	2	-2	0
{1 m ₁₀₀ 0}	1	-1	0	1	-1	0	2	-2	0
{U _z (θ) 1 0}	1	1	2	1	1	2	$2\omega_S$	$2\omega_S$	$4\omega_S$
{U _z (θ) 2 ₀₀₁ 0}	1	1	-2	1	1	-2	$2\omega_S$	$2\omega_S$	$-4\omega_S$
{U _z (θ) m ₀₁₀ 0}	1	-1	0	1	-1	0	$2\omega_S$	$-2\omega_S$	0
{U _z (θ) m ₁₀₀ 0}	1	-1	0	1	-1	0	$2\omega_S$	$-2\omega_S$	0
{U _n (π) 1 0}	1	1	2	-1	-1	-2	0	0	0
{U _n (π) 2 ₀₀₁ 0}	1	1	-2	-1	-1	2	0	0	0

$\{U_n(\pi)\ m_{010} 0\}$	1	-1	0	-1	1	0	0	0	0
$\{U_n(\pi)\ m_{100} 0\}$	1	-1	0	-1	1	0	0	0	0

However, irrep $Q_{3,A}^{1/2} Q_{4,A}^{1/2}(4)$ is always a restricted irrep of any enhanced groups of $G_{H_A^0}^Q$ according

to the compatible relation. In other words, the lift of the quadruply degenerate band β into β_1 and β_2 and the different magnitude of band splitting between α , β_1 , and α , β_2 cannot be described using any enhanced group of $G_{H_A^0}^Q$. As a result, the traditional approach of quasi-symmetry groups based on the unperturbed SOC-free Hamiltonian and the perturbed first-order SOC term fails in describing partially lifted band degeneracy (gapless between α , β_1 v.s. gapped between α , β_2).

C. New approach towards partially lifted degeneracy

To expand the scope of quasi-symmetry group theory in explaining the SOC-induced partially lifted band degeneracy in NdBiPt, we first consider which terms between band α and β support band splitting when the perturbed term H_A' is included. For the $L_z S_z$ term, $\langle \alpha | L_z S_z | \alpha \rangle$ is $G_{H_A^0}^Q$ -forbidden, while $\langle \beta | L_z S_z | \beta \rangle$ is $G_{H_A^0}^Q$ -allowed splitting as given in Eqs. (S5) and (S6), respectively.

$$\langle \alpha | L_z S_z | \alpha \rangle \sim Q_{1,A}^{1/2} \otimes Q_{2,A}^{0-} \otimes Q_{1,A}^{1/2} = Q_{2,A}^{0+} + Q_{2,A}^{0-} + Q_{2,A}^1 \quad (\text{Equation S5})$$

$$\begin{aligned} \langle \beta | L_z S_z | \beta \rangle &\sim Q_{3,A}^{1/2} Q_{4,A}^{1/2} \otimes Q_{2,A}^{0-} \otimes Q_{3,A}^{1/2} Q_{4,A}^{1/2} \\ &= 2Q_{1,A}^{0+} + 2Q_{2,A}^{0+} + 2Q_{1,A}^{0-} + 2Q_{2,A}^{0-} + 2Q_{1,A}^1 + 2Q_{2,A}^1 \end{aligned} \quad (\text{Equation S6})$$

For the $L_+ S_- + L_- S_+$ term, $\langle \alpha | L_+ S_- + L_- S_+ | \alpha \rangle$ and $\langle \beta | L_+ S_- + L_- S_+ | \beta \rangle$ are both $G_{H_A^0}^Q$ forbidden as given in Eqs. (S7) and (S8), respectively.

$$\begin{aligned} \langle \alpha | L_+ S_- + L_- S_+ | \alpha \rangle &\sim Q_{1,A}^{1/2} \otimes (Q_{3,A}^{0+} Q_{4,A}^{0+} + Q_{3,A}^{0-} Q_{4,A}^{0-}) \otimes Q_{1,A}^{1/2} \\ &= 2Q_{3,A}^{0+} Q_{4,A}^{0+} + 2Q_{3,A}^{0-} Q_{4,A}^{0-} + 2Q_{3,A}^1 Q_{4,A}^1 \end{aligned} \quad (\text{Equation S7})$$

$$\begin{aligned} \langle \beta | L_+ S_- + L_- S_+ | \beta \rangle &\sim Q_{3,A}^{1/2} Q_{4,A}^{1/2} \otimes (Q_{3,A}^{0+} Q_{4,A}^{0+} + Q_{3,A}^{0-} Q_{4,A}^{0-}) \otimes Q_{3,A}^{1/2} Q_{4,A}^{1/2} \\ &= 8Q_{3,A}^{0+} Q_{4,A}^{0+} + 8Q_{3,A}^{0-} Q_{4,A}^{0-} + 8Q_{3,A}^1 Q_{4,A}^1 \end{aligned} \quad (\text{Equation S8})$$

Note that $\langle \alpha | L_z S_z | \alpha \rangle$ and $\langle \alpha | L_z S_z | \beta \rangle$ are both $G_{H_A^0}^Q$ -forbidden, while $\langle \beta | L_z S_z | \beta \rangle$ is $G_{H_A^0}^Q$ -allowed splitting. Then we can include the $L_z S_z$ term in the unperturbed Hamiltonian to split off the quadruply degenerate band β into two doubly degenerate band β_1 and β_2 and does not contribute to the band splitting between α and β (α , β_1 and α , β_2).

Table S4. Character table of the little group $G_{H_B^0}^Q = \overline{\mathbf{4}}^2 \mathbf{m}^m \mathbf{2}^\infty \mathbf{1}$, where $\omega_S = \cos m_S \theta$, m_S is the spin

angular momentum. Only unitary group elements are shown here.

	$Q_{1,B}^{0+}$	$Q_{1,B}^{0-}$	$Q_{2,B}^{0+}$	$Q_{2,B}^{0-}$	$Q_{1,B}^{m_S}$	$Q_{2,B}^{m_S}$
{1 1 0}	1	1	1	1	2	2
{1 2 ₀₀₁ 0}	1	1	-1	-1	2	-2
{U _n (π) m ₁₀₀ 0}	1	-1	1	-1	0	0
{U _n (π) m ₀₁₀ 0}	1	-1	-1	1	0	0
{U _z (θ) 1 0}	1	1	1	1	2ω _S	2ω _S
{U _z (θ) 2 ₀₀₁ 0}	1	1	-1	-1	2ω _S	-2ω _S

The unperturbed Hamiltonian $H_B^0 = H_A^0 + \lambda L_z S_z$ breaks all the in-plane unlocked symmetries of $G_{H_A^0}^Q = {}^m\bar{4}^1 m^m 2^\infty 1$, resulting in the little group $G_{H_B^0}^Q = {}^{\bar{1}}\bar{4}^2 m^m 2^\infty 1$. The character table of the little group $G_{H_B^0}^Q$ is given in Table S4. At this level, the doubly degenerate band α and the two doubly degenerate bands β_1, β_2 correspond to irreps $Q_{1,B}^{1/2}(2)$ and $Q_{2,B}^{1/2}(2)$, respectively. Now we turn to the band splitting when considering the perturbed term $H'_B = \frac{\lambda}{2}(L_+ S_- + L_- S_+)$. In the little group $G_{H_B^0}^Q = {}^{\bar{1}}\bar{4}^2 m^m 2^\infty 1$, two pairs of band splitting are both allowed.

$$\begin{aligned} \langle \alpha | L_+ S_- + L_- S_+ | \beta_i \rangle &\sim Q_{1,B}^{1/2} \otimes (Q_{2,B}^{0+} + Q_{2,B}^{0-}) \otimes Q_{2,B}^{1/2}, i = 1, 2 \\ &= 4Q_{1,B}^{0+} + 4Q_{1,B}^{0-} + 4Q_{1,B}^1 \end{aligned} \quad (\text{Equation S9})$$

D. Spin-orbit $U(1)$ quasi-symmetry

As we mentioned in the main text, we find that $P_q = \{U_z(\theta) \otimes R_z(\theta)\}$ can serve as quasi-symmetry and is the operation that determines the partial band degeneracy. First, one can easily check that P_q commutes with H'_B , based on the following relations:

$$[L_z, L_\pm] = \pm L_\pm, [S_z, S_\pm] = \pm S_\pm \quad (\text{Equation S10})$$

$$e^{i\theta L_z} L_\pm e^{-i\theta L_z} = e^{\pm i\theta} L_\pm, e^{i\theta S_z} S_\pm e^{-i\theta S_z} = e^{\pm i\theta} S_\pm \quad (\text{Equation S11})$$

$$(e^{i\theta L_z} e^{i\theta S_z}) L_z S_z (e^{i\theta L_z} e^{i\theta S_z})^{-1} = L_z S_z \quad (\text{Equation S12})$$

$$(e^{i\theta L_z} e^{i\theta S_z}) L_+ S_- (e^{i\theta L_z} e^{i\theta S_z})^{-1} = e^{i\theta} L_+ e^{-i\theta} S_- = L_+ S_- \quad (\text{Equation S13})$$

$$(e^{i\theta L_z} e^{i\theta S_z}) L_- S_+ (e^{i\theta L_z} e^{i\theta S_z})^{-1} = e^{-i\theta} L_- e^{i\theta} S_+ = L_- S_+ \quad (\text{Equation S14})$$

As a result, P_q commutes with $L_z S_z$ and $L_+ S_- + L_- S_+$, i.e., $[e^{i\theta L_z} e^{i\theta S_z}, L_z S_z] = 0$ and $[e^{i\theta L_z} e^{i\theta S_z}, L_+ S_- + L_- S_+] = 0$, respectively.

In addition, P_q transforms different band splitting terms between α and β_1 as:

$$(e^{i\theta L_z} e^{i\theta S_z}) \langle l_0, \uparrow | H'_B | l_+, \uparrow \rangle (e^{i\theta L_z} e^{i\theta S_z})^{-1} \rightarrow e^{i\theta} \langle l_0, \uparrow | H'_B | l_+, \uparrow \rangle \quad (\text{Equation S15})$$

$$(e^{i\theta L_z} e^{i\theta S_z}) \langle l_0, \downarrow | H'_B | l_+, \uparrow \rangle (e^{i\theta L_z} e^{i\theta S_z})^{-1} \rightarrow e^{2i\theta} \langle l_0, \downarrow | H'_B | l_+, \uparrow \rangle \quad (\text{Equation S16})$$

$$(e^{i\theta L_z} e^{i\theta S_z}) \langle l_0, \uparrow | H'_B | l_-, \downarrow \rangle (e^{i\theta L_z} e^{i\theta S_z})^{-1} \rightarrow e^{-2i\theta} \langle l_0, \uparrow | H'_B | l_-, \downarrow \rangle \quad (\text{Equation S17})$$

$$(e^{i\theta L_z} e^{i\theta S_z}) \langle l_0, \downarrow | H'_B | l_-, \downarrow \rangle (e^{i\theta L_z} e^{i\theta S_z})^{-1} \rightarrow e^{-i\theta} \langle l_0, \downarrow | H'_B | l_-, \downarrow \rangle \quad (\text{Equation S18})$$

and the band splitting term between α and β_2 as:

$$(e^{i\theta L_z} e^{i\theta S_z}) \langle l_0, \uparrow | H'_B | l_+, \downarrow \rangle (e^{i\theta L_z} e^{i\theta S_z})^{-1} \rightarrow \langle l_0, \uparrow | H'_B | l_+, \downarrow \rangle \quad (\text{Equation S19})$$

$$(e^{i\theta L_z} e^{i\theta S_z}) \langle l_0, \downarrow | H'_B | l_+, \downarrow \rangle (e^{i\theta L_z} e^{i\theta S_z})^{-1} \rightarrow e^{i\theta} \langle l_0, \downarrow | H'_B | l_+, \downarrow \rangle \quad (\text{Equation S20})$$

$$(e^{i\theta L_z} e^{i\theta S_z}) \langle l_0, \uparrow | H'_B | l_-, \uparrow \rangle (e^{i\theta L_z} e^{i\theta S_z})^{-1} \rightarrow e^{-i\theta} \langle l_0, \uparrow | H'_B | l_-, \uparrow \rangle \quad (\text{Equation S21})$$

$$(e^{i\theta L_z} e^{i\theta S_z}) \langle l_0, \downarrow | H'_B | l_-, \uparrow \rangle (e^{i\theta L_z} e^{i\theta S_z})^{-1} \rightarrow \langle l_0, \downarrow | H'_B | l_-, \uparrow \rangle \quad (\text{Equation S22})$$

Based on Eqs. (S15)~(S22), we can conclude that the spin-orbit $U(1)$ symmetry $P_q = \{U_z(\theta) \parallel R_z(\theta)\}$ is indeed a quasi-symmetry emerged in α and β_1 bands and the quasi-symmetry group is $\mathcal{Q}(G_{H'_B}^Q, P_q) = {}^1\infty/\bar{1}m^2m^\infty 1$. The character table of the little group $\mathcal{Q}(G_{H'_B}^Q, P_q)$ is given in Table S5. The selection rules for $\Delta E_{\alpha\beta_1}$ and $\Delta E_{\alpha\beta_2}$ are now characterized by two corresponding components, as

$$\langle \alpha | H'_B | \beta_1 \rangle \sim Q_Q^{1/2,0} \otimes (Q_Q^{0+} + Q_Q^{0-}) \otimes Q_Q^{1/2,1} = 2Q_Q^{0,1} \oplus 2Q_Q^{1,1} \quad (\text{Equation S23})$$

$$\langle \alpha | H'_B | \beta_2 \rangle \sim Q_Q^{1/2,0} \otimes (Q_Q^{0+} + Q_Q^{0-}) \otimes Q_Q^{1/2,0} = 2(Q_Q^{0+} \oplus Q_Q^{0-} \oplus Q_Q^{1,0}) \quad (\text{Equation S24})$$

Here, only $\langle \alpha | H'_B | \beta_2 \rangle$ is $\mathcal{Q}(G_{H'_B}^Q, P_q)$ -allowed splitting. Therefore, the band crossing by α and β_2 is lifted by H'_B with a 672.4 meV gap.

Table S5. Character table of the little group $\mathcal{Q}(G_{H'_B}^Q, P_q) = {}^1\infty/\bar{1}m^2m^\infty 1$, where $\omega_S = \cos m_S \theta$, $\omega_L = \cos m_L \theta$, $\omega_{L+S} = \cos(m_L + m_S)\theta$. m_S and m_L are the spin and the orbital angular momentum, respectively. Only unitary group elements are shown here. $C_z(\theta)$ denotes the continuous lattice rotation along the z axis.

	Q_Q^{0+}	Q_Q^{0-}	$Q_Q^{m_S, m_L}$
$\{1\ 1 0\}$	1	1	2
$\{1\ C_z(\theta) 0\}$	1	1	$2\omega_L$
$\{U_z(\theta)\ 1 0\}$	1	1	$2\omega_S$

$\{U_z(\theta)\ C_z(\theta) 0\}$	1	1	$2\omega_{L+S}$
$\{U_n(\pi)\ m_{100} 0\}$	1	-1	0

E. The $k \cdot p$ model of NdBiPt

To validate the above quasi-symmetry analysis, a $k \cdot p$ model was developed in the vicinity of the Γ point. Following the analysis of the orbital-projected band, a linear combination of the s and p_z orbitals was utilized as the basis functions to describe the α band. Thus, these basis functions can be denoted as $|l_0\rangle = \theta|s\rangle + \gamma|p_z\rangle$. Likewise, for the β band, a linear combination of the p_x , p_y , d_{xz} , and d_{yz} orbitals was selected as the basis functions, represented as $|l_{\pm}\rangle = \frac{1}{\sqrt{2}}(|u_x\rangle \pm i|u_y\rangle)$, $|u_{x/y}\rangle = \eta|p_{x/y}\rangle + \delta|d_{xz/yz}\rangle$. Under these two sets of basis functions, the Hamiltonian is expressed as a 6×6 matrix,

$$H_0 = \begin{pmatrix} \varepsilon_0 & 0 & 0 \\ 0 & \varepsilon_1 & 0 \\ 0 & 0 & \varepsilon_2 \end{pmatrix} \otimes \sigma_0, \quad (\text{Equation S25})$$

where $\varepsilon_0 = \frac{(k_x^2+k_y^2)}{2m_0^{xy}} + \frac{k_z^2}{2m_0^z} + \mu_0$, $\varepsilon_1 = \frac{(k_x^2+k_y^2)}{2m_1^{xy}} + \frac{k_z^2}{2m_1^z} + \mu_1$, $\varepsilon_2 = \frac{(k_x^2+k_y^2)}{2m_2^{xy}} + \frac{k_z^2}{2m_2^z} + \mu_2$. m_i^{xy} and m_i^z denote the effective masses of the band i along the xy direction and the z direction, respectively, while μ_i denotes a constant of energy.

We further consider the first-order SOC term, and the corresponding Hamiltonian can be written as,

$$H_{soc}^{(1)} = \lambda L \cdot S = \lambda L_z \cdot S_z + \frac{\lambda}{2}(L_+S_- + L_-S_+), \quad (\text{Equation S26})$$

where λ denotes the strength of SOC. L_{\pm} (S_{\pm}) is the orbital (spin) step-up/step-down operator. In our basis $\{|l_0, \uparrow\rangle, |l_0, \downarrow\rangle, |l_-, \uparrow\rangle, |l_-, \downarrow\rangle, |l_+, \uparrow\rangle, |l_+, \downarrow\rangle\}$, the corresponding matrix is given by

$$H_{soc}^{(1)} = (h_{ij})_{6 \times 6} = \lambda \begin{pmatrix} 0 & 0 & 0 & \sqrt{2}/2 & 0 & 0 \\ 0 & 0 & \sqrt{2}/2 & 0 & 0 & 0 \\ 0 & \sqrt{2}/2 & -1/2 & 0 & 0 & 0 \\ \sqrt{2}/2 & 0 & 0 & -1/2 & 0 & 0 \\ 0 & 0 & 0 & 0 & 1/2 & 0 \\ 0 & 0 & 0 & 0 & 0 & 1/2 \end{pmatrix}, \quad (\text{Equation S27})$$

where h_{ij} represents the element in the i th row and j th column of $H_{soc}^{(1)}$. Incorporating this additional term into the complete Hamiltonian leads to the derivation of a 6×6 matrix for every Bloch vector k . From this analysis, we can derive band structure with SOC (see Fig. S10). In Fig. S10, we show that our $k \cdot p$ model can be fitted to describe the band structure from DFT calculation. Moreover, the $\Delta E_{\alpha\beta_1}$ arises from the hybridization between the β_1 and α bands, whereas $\Delta E_{\alpha\beta_2}$ originates from the hybridization between the β_2 and α bands. Here α , β_1 , and β_2 bands are defined as:

$$\begin{cases} \alpha = (|l_0, \uparrow\rangle + |l_0, \downarrow\rangle)/\sqrt{2} \\ \beta_1 = (|l_+, \uparrow\rangle + |l_-, \downarrow\rangle)/\sqrt{2} \\ \beta_2 = (|l_-, \uparrow\rangle + |l_+, \downarrow\rangle)/\sqrt{2} \end{cases} \quad (\text{Equation S28})$$

The distinction between the two pairs can be determined utilizing the SOC Hamiltonian Eq. (S27),

$$\Delta E_{\alpha\beta_1}^{(1)} \sim \langle \alpha | H_{soc}^{(1)} | \beta_1 \rangle = \lambda/2(h_{15} + h_{25} + h_{16} + h_{26}) = 0 \quad (\text{Equation S29})$$

$$\Delta E_{\alpha\beta_2}^{(1)} \sim \langle \alpha | H_{soc}^{(1)} | \beta_2 \rangle = \lambda/2(h_{13} + h_{23} + h_{14} + h_{24}) = \sqrt{2}\lambda/2. \quad (\text{Equation S30})$$

Therefore, the first-order SOC effect is prohibited for the $\Delta E_{\alpha\beta_1}$, whereas it is allowed for the $\Delta E_{\alpha\beta_2}$. As a result, the $\Delta E_{\alpha\beta_1}$ is two orders of magnitude smaller than $\Delta E_{\alpha\beta_2}$. This result is consistent with quasi-symmetry analysis, further demonstrating the topological charge quadrupole is protected by spin-orbit $U(1)$ quasi-symmetry.

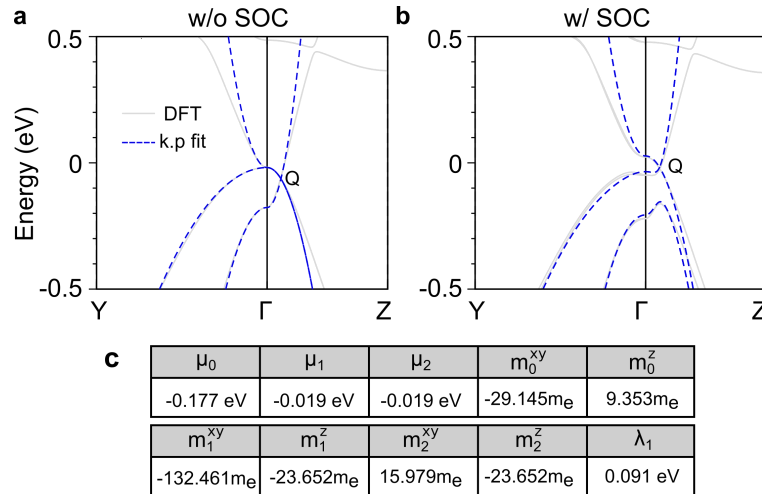


Fig. S10. The band structures of NdBiPt calculated by $k \cdot p$ model and DFT. a and b denote the electronic structure of NdBiPt without SOC and with SOC ($\lambda = 0.2$), respectively. The blue and the gray lines represent the results from $k \cdot p$ model and DFT calculation, respectively. The $k \cdot p$ model's fitting parameters are listed in c.